Alma Mater Studiorum · University of Bologna

School of Science

Department of Physics and Astronomy

Bachelor Degree in Physics

A MicroStrip Detector study on track reconstruction at the FOOT experiment

Supervisor:

Dott. Matteo Franchini

Co-supervisor:

Dott. Giacomo Ubaldi

Submitted by:

Giulia Cicogna

Academic Year 2022/2023

A Bianca e Valeria

Abstract

The FOOT experiment contributes to advancing research in the field of hadrontherapy, an innovative oncological treatment that employs a diverse range of hadronic particles with energies ranging from 100 to 700 MeV. In contrast to conventional radiation therapy using mainly X-ray beams, which unavoidably affect healthy tissues, hadrontherapy precisely delivers the peak of radiation energy to the targeted region, minimizing harm to non-cancerous tissues. However, to optimize this procedure, it is essential to investigate potential nuclear fragmentation processes occurring between the biological tissue and the utilized particle beam, and here stands precisely the focus of the FOOT experiment.

The thesis project presented primarily revolves around the reconstruction of points and tracks within the MSD detector, alongside data selection processes, and it relies on MonteCarlo data simulating the interaction between an oxygen beam with an energy of 400 MeV/u and a carbon target. There are two primary objectives in this study, given that true and ghost points represent real and spurious hit points in the detector: first, to accurately reconstruct MSD points and differentiate them between ghost and true points, and second, to reconstruct MSD tracks and effectively discriminate between true and ghost tracks. This project also focuses on the measurement of the efficiency and purity parameters of the data selection method implemented. For points, efficiency and purity values obtained are 90.54% (and its uncertainty of 0.02%) and 97.59%, respectively, while for tracks, efficiency is 92.27% (and its uncertainty of 0.02%) and purity is 42.34%.

Sommario

L'esperimento FOOT si occupa della ricerca in adroterapia, un innovativo trattamento oncologico che utilizza una vasta gamma di particelle adroniche con energie comprese tra 100 e 700 MeV/u. A differenza della radioterapia convenzionale, che utilizza principalmente raggi X e che inevitabilmente colpisce i tessuti sani, l'adroterapia offre la possibilità di determinare con precisione il picco di energia radiativa nel bersaglio, riducendo al minimo i danni ai tessuti non tumorali. Tuttavia, per ottimizzare questa procedura, è essenziale analizzare i possibili processi di frammentazione nucleare che avvengono tra il tessuto biologico e il fascio di particelle utilizzato. Proprio in questo risiede l'obiettivo principale di FOOT.

Il progetto di tesi presentato di seguito si basa sulla ricostruzione di punti e tracce all'interno del rivelatore MSD e utilizza dati MonteCarlo che simulano l'interazione tra un fascio di ossigeno con un'energia di 400 MeV/u e un bersaglio di carbonio.

Definendo i punti true e ghost come punti reali e spuri rispettivamente, sono due gli obiettivi principali: primo, ricostruire con precisione i punti dell'MSD e distinguere tra punti ghost e punti true; secondo, ricostruire le tracce dell'MSD e cercare un discriminante tra tracce vere e ghost. Per fare ciò, è stato utile valutare l'efficienza e la purezza durante la selezione dei dati. Per i punti, sono stati ottenuti valori di efficienza e purezza pari al 90.54% (con un'incertezza del 0.02%) e al 97.59%, rispettivamente, mentre, per le tracce, si sono ottenuti valori di efficienza del 92.27% (con un'incertezza del 0.02%) e una purezza del 42.34%.

Indice

Introduction

Cancer is a complex group of diseases that affect millions of lives worldwide. It poses a significant health challenge in our modern society, being the second leading cause of death after cardiovascular diseases. Although the causes of the insurgence of this disease can be various, it is generally characterized by the uncontrolled growth and spread of abnormal cells in the body, leading to the formation of malignant tumors. Over the years, extensive research and advancements in medical science have provided various treatment options for cancer, such as the long-established modalities of surgery, chemotherapy, immunotherapy, radiotherapy, and a relatively new modality of hadrontherapy.

Both radiotherapy and hadrontherapy exploit radiation to expose the tumoral mass. While radiotherapy employs high-energy electromagnetic radiation (mainly X-rays), hadrontherapy uses charged particles, such as protons or heavy ions; this radiative exposure targets and destroys cancer cells. While electromagnetic radiation predominantly releases its energy in the surface layers of tissue, charged particles release their energy precisely within the tumor at a depth known as the Bragg peak.

Hence, in situations where conventional radiotherapy may not be suitable due to its specific advantages and limitations, hadrontherapy provides a means to minimize harm to the healthy tissues surrounding the tumor, all the while effectively targeting and causing significant damage to the cancerous tissues that require eradication. This capability allows for the application of hadrontherapy even in tissues situated in close proximity to vital organs, consequently diminishing the risk of damage to these critical structures.

Although hadrontherapy originated as a concept in the mid-20th century, it has firmly established itself as a cancer treatment modality in recent years. By the end of 2021, more than 300,000 patients had received hadrontherapy treatment, according to reports from [1]. Furthermore, the number of facilities equipped to provide hadrontherapy using both protons and carbon ions has expanded through the years to reach the current total of 94.

In Italy, there are three main operational centers of this nature. Firstly, there is the CATANA center (Centro di AdroTerapia ed Applicazioni Nucleari Avanzate), situated at the National

Laboratories of the South in Catania, which is the sole facility where ocular region tumors can be treated. Then, the CNAO (Centro Nazionale di Adroterapia Oncologica) is present. Located in Pavia, this latter is the only facility in Italy capable of offering hadrontherapy treatments using both protons and carbon ions. Worldwide, there are only six such facilities. Lastly, there is the Proton Therapy Center in Trento.

Although clinical data from these facilities are reassuring, currently, hadrontherapy cannot establish a standardized treatment protocol due to the lack of precise knowledge regarding potential side effects resulting from nuclear interactions between the beam and human body nuclei. For this reason, in 2017, the INFN (Istituto Nazionale di Fisica Nucleare) approved the FOOT experiment.

The FOOT (FragmentatiOn Of Target) experiment aims to enhance the experimental landscape to improve clinical treatment planning systems. Specifically, the technical goal of FOOT is to measure the differential cross-section of all fragments generated during the nuclear interaction between the projectile beam and the target, achieving a precision level of less than 5%. Moreover, in addition to its collaboration with numerous international research groups, FOOT is also engaged in the exploration of space radioprotection.

The aim of this thesis is to investigate the reconstruction of points and tracks within a specific part of the FOOT experimental apparatus, namely the MicroStrip Detector (MSD). This study is computational in nature and, more specifically, seeks to develop an effective method for discriminating between real points and tracks from those that are of spurious origin during the reconstruction process.

The subsequent thesis unfolds across four distinct chapters.

Chapter 1 introduces some fundamentals of radiobiology following a brief overview of current oncological therapies. It also delves into the underlying physical phenomena of treatments and explores the interactions between radiation beams and charged particles and matter.

Chapter 2 presents the FOOT experiment and its experimental setup.

Chapter 3 discusses the code tools and results related to the study of reconstructed points in the MSD. Specifically, it distinguishes between points defined as true and those classified as ghost, of spurious nature.

Chapter 4 addresses track reconstruction, following a similar approach to the previous chapter, and aiming to discriminate between true and ghost tracks associated with points.

1. An Introduction to Hadrontherapy

The first-ever document suggesting the idea of exploiting heavy charged particles for cancer treatment was an article drafted in 1946 by accelerator pioneer and Fermilab founder Robert R. Wilson. Seventy-seven years have passed and cancer still poses a threat, representing the second-highest cause of death in developed countries as well as resulting in an undeniable challenge in its medical treatment. Wilson did not know though that via his article *Radiological Use of Fast Protons* he would pave the way for the development of innovative and high-precision oncologic therapy of hadrontherapy. The devastating impact of cancer goes way beyond its status as a well-known and leading cause of death. Cancer permeates and disrupts the natural stability underlying biological tissues, causing substantial alterations concerning both physiological and structural aspects. It is usually correlated to unrestrained cell proliferation and division, impairment of neighboring vital organs and tissues, and metastasis, the spread of cancer beyond its initial site of origin. In its relentlessness, cancer advances in its ability to control essential biological mechanisms, thus resulting in a menacing challenge for medicine in its treatment. For this reason, a brief overview of the biological repercussions induced by cancer in tissues and cells is needed.

1.1 Cancer's Impact on Biological Tissues

The human body is an intricate and wondrous living machine, and as such it is constituted of smaller components that work together in harmony performing various vital tasks that are crucial in defining life, such as digesting nutrients and breathing, through specialized structures, namely organs. These smaller living units are cells and in this sense, they represent the fundamental unit of life. In order to maintain this harmony and ensure the proper functioning of each organ, it is necessary for damaged or aging cells to be replaced, and for specific types of cells to proliferate in response to changes in the environment. It is important to underline that cell proliferation in standard circumstances is a highly regulated process along with cell growth and inheritance, which are controlled by the cellular deoxyribonucleic acid, i. e. DNA. DNA is a double-helix structured molecule composed of a sequence of nucleotides, each consisting of

a phosphate group, a deoxyribose sugar molecule, and a nitrogenous base, that resides in one specific cellular organelle, the nucleus, containing the information that regulates the development and reproduction of biological organisms. Within human cells, the DNA is organized into 46 chromosomes, which are arranged in pairs, just as genes, and each individual chromosome belonging to a particular pair originates from each biological parent. Genes are specific segments of DNA that occupy a designated location on a chromosome and provide instructions, through biochemical mechanisms, for producing proteins, which are substantial for various cellular processes. As mentioned before, cellular reproduction is a highly controlled process, for it occurs only in response to specific signals from growth factors from a biochemical perspective. When a cell receives the signal to divide, it enters the cell cycle that consists of different phases and includes controls along various cycle stages to guarantee its proper progression. Any disruptions or errors during this process can lead to the development of cancerous cells. Cancer is the product of the long and multi-step process of oncogenesis, that is responsible for turning cells into cancerous cells. The nature of oncogenesis resides in the plasticity and versatility of metazoan tissues because it presupposes the ability of many cells to participate in tissue morphogenesis even after the development of the organism. These same cells have the potential to acquire genomic information that is typically restricted to them, leading them to assume roles that are unsuitable for normal tissue maintenance and function while also often subjecting their genomes to corruptive alterations through various mechanisms that result in mutations of the genome, and therefore causing cells to acquire abnormal phenotypes. In this sense, tumor cells arise from normal tissue and result from disrupted normal development. While normal cells are programmed to cooperate to assure organismic survival, cancer cells possess a sole objective, that is purely centered on proliferating.

Significant differences existing between tumoral and non-defective cells are the following:

Growth Control Growth in cells is usually finely regulated and, as a consequence, cell division results in a heavily controlled process, while cancerous cells exhibit uncontrolled growth, proliferating swiftly without restraint.

Contact Inhibition of Proliferation Normal cells demonstrate contact inhibition, a phenomenon where they halt the cell cycle, inducing a decrease in proliferation, when a higher density is reached or when neighboring cells come in contact with them. This response is fundamental to the proper development or repair of tissues, differentiation, and morphogenesis.

Cancerous cells, in contrast, typically lose this ability resulting in the invasion of surrounding tissues and metastasis.

Differentiation Cells typically differentiate into specialized cell types associated with distinct functions and characteristics while cancer cells are undifferentiated or poorly differentiated compromising their ability to perform specialized functions.

Apoptosis Normal cells experience a programmed form of death called apoptosis when they are damaged or it is necessary for tissue homeostasis; cancer cells avoid apoptosis, thriving and accumulating as a result.

DNA Repair Mechanisms Efficient DNA repair mechanisms are typical to normal cells and are able to correct errors and corruptions in their genes. Cancer cells show repair mechanisms that are impaired causing the increase of genetic mutations that accommodate their uncontrolled growth.

Immune Response Cells usually can be identified and eventually eliminated if deemed abnormal by the immune system, while cancer cells can evade immune detection and suppression, allowing them to proliferate freely.

Other interesting aspects may concern cellular adherence, which is reduced for cancer cells enabling them to detach from their initial location of origin, genetic instability, and energy metabolism.

In conclusion, the biological impact of cancer on tissues seems to be just as complex and multifaceted, affecting the normal processes of cells, organs, and the entire organism and often leading to the formation of tumors, lumps and abnormal masses of tissue, which can hinder the standard functionality and integrity of the organism. Different tailored therapies can be employed after cancer formation to eliminate defective cells and interrupt abnormal processes. These treatments vary depending on a multitude of factors, such as tumor locations, tumor types, metastasis stage, or also physiological features of the host.

1.2 Modern Approaches for Cancer Treatment

Modern oncologic treatment approaches often involve combined modalities, each tailored to the disease's and the patient's characteristics. Such modalities include surgery, radiation therapy, chemotherapy, immunotherapy, and hormonal therapy.

Radiation Therapy It plays a fundamental role in cancer treatment being employed for approximately half of all oncologic patients in their treatment journey and contributing to almost 40% of curative treatment for cancer. Its main aim consists of damaging the genetic material of cancer cells, while also trying to limit any possible detrimental effects on healthy tissues, thus depriving them of their ability to grow and further divide by directing high-energy photon-based radiation (usually X-rays) to targeted bodily areas that are affected by cancer.

Hadrontherapy Also known as Charged Particle Therapy, hadrontherapy is an innovative approach to cancer radiotherapy that harnesses multidirectional irradiation of charged nuclear particles, such as protons and light ions which release their energy at a specific depth within the tissues, to address both early and advanced tumors. Whereas in regular radiation therapy, inevitably, healthy tissue is also irradiated, in hadrontherapy the peak of the radiation energy is released in a precise region, deeply hindering damage to non-cancerous tissues.

Two extensively used concepts in radiation oncology to assess the potential effects of radiation on normal tissue and tumor control are NTCP (Normal Tissue Complication Probability) and TCP (Tumor Control Probability). NTCP quantifies the likelihood of the occurrence of complications in healthy tissues due to radiation exposure, while TCP estimates the probability of achieving successful tumor control through radiotherapy. In essence, the foundation of radiotherapy hinges on the intricate balance between these two factors and also on the knowledge that healthy cells possess a greater ability to withstand radiation and repair the consequent damage. For this very reason, radiotherapy or hadrontherapy sessions are scheduled at distinct intervals, allowing the body to mend the healthy tissues that are inevitably affected by irradiation. This approach is favored over oncogenic tissues, which require more extended recovery times. Enhancing its effectiveness involves manipulating various stages of the cell's life cycle, while allowing ample time for healthy tissues to undergo repair.

1.2.1 DNA Damage

In general, it can be said that radiation therapy, which unintentionally becomes a concerning perturbance of healthy tissues, instigates processes where DNA damage assumes significance due to the ionizing radiation's potential to breach cellular genetic integrity. The high-energy particles released during radiotherapy interact with DNA molecules, resulting in direct breakage, or cross-linkages, within DNA strands and generation of free radicals, or rather chemically unstable molecules with unpaired electrons that trigger a chain reaction of oxidative stress and further expand the damage brought upon the DNA structure.

Given that the cells constituting the human body are predominantly composed of water, the interaction of radiation or charged particles on water molecules initiates ionization, leading to the release of an ion and an electron.

$$H_2O \rightarrow H_2O^+ + e^- \tag{1.1}$$

Subsequently, the free electron generates a negatively charged ion by binding with another water molecule.

$$H_2O + e^- \rightarrow H_2O^- \tag{1.2}$$

In both scenarios, the H_2O^+ and H_2O^- ions exhibit instability, leading to radiolysis, a process where they undergo fragmentation, thus producing free radicals.

$$\begin{aligned} H_2O^+ &\rightarrow H^+ + OH\cdot \\ H_2O^- &\rightarrow H\cdot + OH^- \end{aligned} \tag{1.3}$$

The unpaired electrons possessed by these prompt their active engagement in reactions to either relinquish or share the excess electron, thus rendering them both oxidants, accepting electrons, and reducers, donating electrons. As a matter of fact, $OH\cdot$ and $H\cdot$ can either recombine to

engender water molecules or generate oxygen peroxides.

$$OH \cdot + OH \cdot \rightarrow H_2O_2 \tag{1.4}$$

Oxidative stress can lead to DNA damage [3] through processes like Fenton reaction (1.5), ultimately resulting in strand breaks, base damage, and other disruptions in DNA that can induce mutations, chromosome deletions, and other genetic abnormalities.

$$\begin{aligned} Fe^{2+} + H_2O_2 &\rightarrow Fe^{3+} + \cdot OH + OH^- \\ Fe^{3+} + H_2O_2 &\rightarrow Fe^{2+} + \cdot OOH + H^+ \end{aligned} \tag{1.5}$$

This sequence of damage triggers sets off a series of cellular reactions, encompassing the activation of DNA repair mechanism and, in severe scenarios, programmed cell death, or apoptosis. Cellular defenses indeed include DNA repair mechanisms, notably DNA polymerase whose duty is precisely that to mend one DNA strand after some form of impairment by constructing the complementary bases with the information of the opposite strand's nitrogenous bases. Therefore, to induce irremediable breakage to DNA one must employ radiation with a highly intense beam causing a double-strand break, preventing DNA repair and interrupting cellular reproduction. Among DNA damage one can thus enumerate single-strand breaks, double-strand breaks, and spurious cross-linkages. Repair enzymes can often rectify damage, but excessive exposure to ionizing radiation can push beyond their capacity. Such damage can lead to cell death or, in unique scenarios, cell survival with reduced genetic material, potentially contributing to cancer formation. Understanding these dynamics is crucial for optimizing both therapeutic strategies and radiation safety.

Before delving into the physics underlying the foundation of hadrontherapy, it is necessary to establish some pivotal insights into dosimetry, which is the scientific discipline that allows, within the domains of health physics and radiation protection, to evaluate the radiation absorption within human tissues during medical procedures like radiation therapy.

1.3 Dosimetry Fundamentals

The harmful effects of radiation can be broadly classified into two categories, that are stochastic effects and non-stochastic effects, both of which are fundamental to understanding the impact of radiation on human health based on various connected factors such as the nature of radiation, the amount and the duration of exposure.

Non-stochastic Effects Also known as deterministic effects, these emerge when a precise dose threshold is exceeded. In other words, once this threshold is reached, some particular effects are certain to manifest with a severity that is directly related to the radiation dose received.

Stochastic Effects Also known as probabilistic effects, they have a probability of occurring with exposure to radiation and are random in nature. Unlike non-stochastic effects, the severity of these effects doesn't depend on the dose level. Instead, as the radiation dose increases, the likelihood of these effects happening becomes higher, while their impact remains constant.

When establishing safety standards and protocols for radiation protection in medical practices and industries must carefully take into account these effects, which are therefore thoroughly examined in vitro studies.

1.3.1 Absorbed Dose

The *absorbed dose* is the quantity that expresses the amount of energy absorbed per unit mass of a considered material, like human tissue, air, water, or any generic material. It is a generic measurement that can be applied to any type of radiation and it is used in radiobiology for its efficiency in estimating the damage caused after the exposure of a specific radiation. The absorbed dose is usually given in the SI unit of the gray (Gy), which is equivalent to one unit of joules per kilogram (J/Kg).

$$D_{ab} = \frac{dE_{ab}}{dm} \tag{1.6}$$

In many applications, it is preferable to measure the absorbed dose per unit of time, which is referred to as the absorbed dose intensity.

1.3.2 Equivalent Dose

Consistently to the findings from radiobiology studies, biological damage can vary depending on the nature of radiation even when the absorbed dose values are comparable. To address the different effectiveness in inducing biological effects varying on the radiation type, the quantity of equivalent dose, whose standard unit is the sievert (Sv), is introduced. This variable, D_{eq}[1], is defined as the average dose of a material multiplied by a dimensionless weight factor, w_R, depending on the radiation type.

$$D_{eq} = \sum_R w_R \, D_{ab,R} \tag{1.7}$$

This enables a more accurate evaluation of the potential biological impact of different radiation types while accounting for their varying levels of ionization. For instance, α radiation is assigned a weighting factor of 20, while X-rays or γ-rays have a weighting factor of 1, thus resulting in the dose equivalent being numerically equal to the absorbed dose (see Table 1.3.2 for further examples).

Radiation Type	$\boldsymbol{w_R}$
Photons	1
β particles	1
Protons	2
α particles	20
Neutrons	2 - 20 depending on energy

Tabella 1.3.2: *Weighting factors for different types of radiation recommended in ICRP, that is the International Commission on Radiological Protection, Publication No. 103 (2007), [4].*

[1]The sum encompasses all types of radiation; w_R represents the weighting factor associated with the radiation nature, while $D_{ab,R}$ stands for the equivalent absorbed dose of the radiation under consideration.

1.3.3 Effective Dose

The likelihood of the occurrence of stochastic effects within a particular tissue or organ, T, is not only influenced by the equivalent dose received by that specific area but also by the inherent sensitivity of the receiving tissue or organ to radiation.

Thus, it is convenient to define an additional parameter, w_T, to account for this aspect that represents the radiation it would receive if the entire body was exposed. It is important to underline how these factors are generic and do not depend on any considered individual subject as they are derived from extensive statistical analyses conducted over years in radiobiology research (see Table 1.3.3 for some examples).

Consequently, let us define the effective dose, D_{ef}[2], as

$$D_{ef} = \sum_T w_T \, D_{eq,T} \tag{1.8}$$

Measurement of both equivalent and effective doses is conducted in sieverts (Sv), a unit that standardizes the impact of one sievert of a particular radiation type or tissue to be on par with that of one gray of γ radiation, which serves as the benchmark radiation model.

Tissue/Organ	$\boldsymbol{w_T}$
Breast	0.12
(Red) Bone Marrow	0.12
Lung	0.12
Stomach	0.12
Liver	0.04
Brain	0.01

Tabella 1.3.3: *Weighting factors for differently radiosensitive tissues or organs enumerated by the International Commission on Radiological Protection (2007), [4]. Each coefficient corresponds to a percentage of the total body (100%), and their collective sum is 1.*

[2]The summation encompasses all tissues, as indicated by T, and $D_{eq,T}$ represents the equivalent dose absorbed by tissue T.

1.3.4 Cell Survival and the Linear Quadratic Model

Cell survival is a crucial concept in radiobiology that refers to the ability of cells to remain viable and functional after exposure to possible death-inducing factors, such as cytotoxic agents or radiation. A useful tool for analyzing this parameter is the cell survival plot that enlightens the relationship between the fraction of surviving cells and the administered dose of the cell-damaging agent. This curve often exhibits a sigmoid shape, as can be observed in Figure 1, when represented on linear scales and when referring to exposure to radiation. In general, to ensure the death of a certain percentage of cells, one can determine the necessary dose: for 90% it would be an effective dose 90%, ED90.

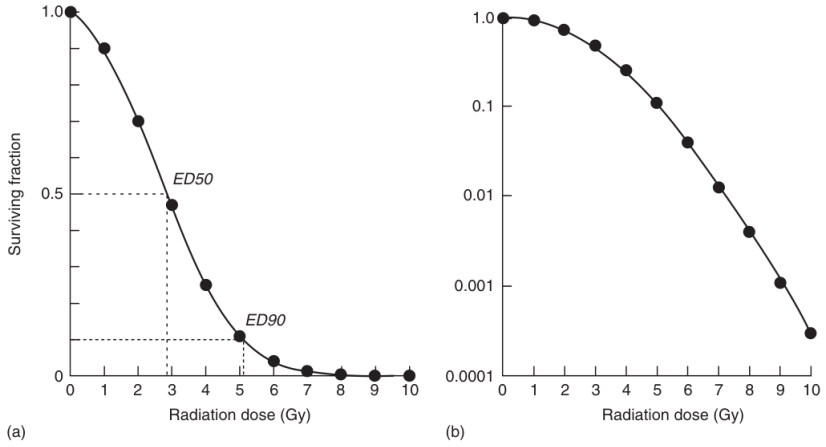

Figure 1: *A conventional cell survival curve, representing cells irradiated in tissue culture, is depicted (a) using a linear scale and (b) a logarithmic scale to illustrate survival rates. Note that in the data presented radiation doses surpassing 5Gy lead to clonogenic cell survival of less than 10%.*

Since a logarithmic scale simplifies the comparison of exceedingly low cell survival rates required for achieving substantial tumor size reduction or control, cell survival curves are commonly represented using a logarithmic scale.

One widely used model to describe cell survival is the Linear Quadratic (LQ) model, whose plot is depicted in Figure 2. It is purely based on mathematics and provides predictions for cell survival in response to varying radiation dose, also accurately describing radiation response in the low-dose region. Let S be the fraction of surviving cells after an administered dose D. Then, it holds true that [5]:

$$
\begin{aligned}
-ln(S) &= \alpha D + \beta D^2 \\
P(Survival) &= e^{-(\alpha D + \beta D^2)}
\end{aligned}
\tag{1.9}
$$

The linear component, αD, signifies the direct correlation between radiation dosage and cell destruction, particularly at lower doses. Conversely, the quadratic component, βD^2, acknowledges the higher cell demise occurring at higher doses, attributed to the complex combination of numerous radiation-triggered lesions to cells and tissues.

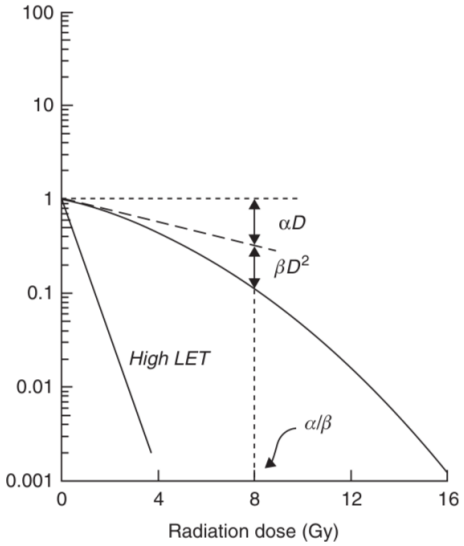

Figure 2: *Curve of LQ Model. Note that the survival curve is continuously bending downward as the radiation dose increases. As a result, the curve never maintains a completely straight trajectory. This characteristic of the curve reflects the intricate relationship between radiation dose and cell survival, which exhibits a gradual decline without a clear threshold value.*

The curvature is primarily dictated by the ratio of α/β, where the dimensions of α are Gy^{-1} and the dimensions of β are Gy^{-2}, resulting in α/β having dimensions of Gy. This ratio represents the dose at which the linear contribution to damage (αD on a logarithmic scale) becomes equivalent to the quadratic contribution (βD^2). In simpler terms, the α/β ratio depicts how well a cell can repair damage caused by radiation, thus indicating its sensitivity to radiation-induced harm.

For cell responses to densely-ionizing radiation such as neutrons or α particles, survival curves are nearly exponential, being the ratio α/β exceptionally high (Figure 3).

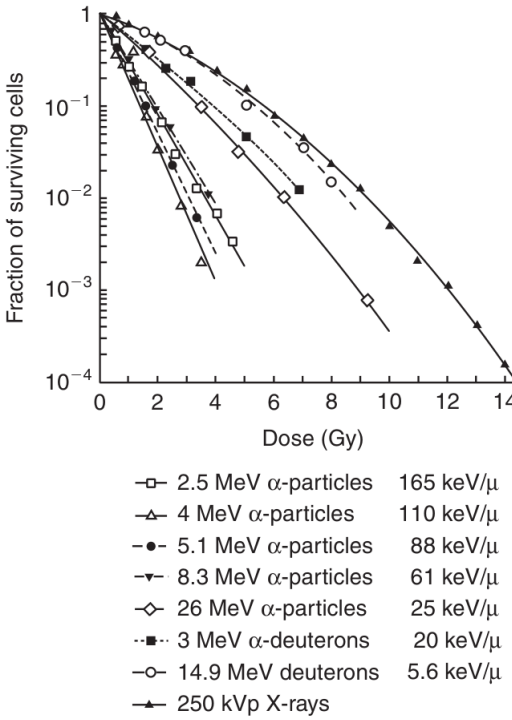

Figure 3: *Viability of human kidney cells following in vitro exposure to various radiation types with different linear energy transfer (LET) values, adapted from [6].*

1.3.5 Linear Energy Transfer

Linear Energy Transfer (LET) refers to the measure of ionization density in the path of particles, quantifying the average energy transferred through collisions by a charged particle while crossing a distance of 1 μm.

$$LET = \frac{dE}{dx} \tag{1.10}$$

For example, γ-rays exhibit a LET of approximately 0.3 $keV/\mu m$ (low-LET), while α-particles possess a LET of around 100 $keV/\mu m$ (high-LET). As LET increases, radiation generates a higher cellular demise per gray of the administered dose, causing survival curves to become steeper and to show reduced shoulders. This, in the context of the LQ model, is equivalent to a higher ratio of lethal to potentially lethal lesions or a higher difficulty in repairing high-LET radiation damage, thus resulting in a higher α/β ratio. Consequently, high-LET radiations generally correspond to responses with elevated α/β values. Remarkably, for particles of identical atomic composition, LET tends to increase as particle energy decreases. However, particles

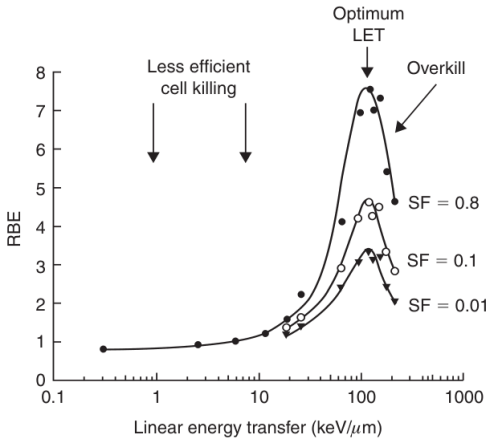

Figure 4: *Variation in relative biological effectiveness (RBE) as a function of linear energy transfer (LET) and the overkill phenomenon occurring due to extremely high LET radiations, with SF being the surviving fraction. .*

possessing a higher LET are less effective due to the phenomenon of overkill, which is shown in Figure 4.

1.3.6 Relative Biological Effectivness

Relative biological effectiveness (RBE) quantifies the ratio of the dose from reference radiation, D_R, to the dose from the test radiation, D_T, that is needed to produce an equivalent biological effect. A common reference low-LET radiations are photons in the X-rays or γ-rays regions.

$$RBE = \frac{D_R}{D_T} \tag{1.11}$$

It is important to underline how RBE isn't a fixed value, but else it fluctuates based on the extent of biological damage, thus hinging on the dose level and the linear energy transfer (LET). The RBE of a particle attains its zenith at a LET around $100 keV/\mu m$, which corresponds to the optimal LET value to reproduce the biological effect needed. Then, it decreases at higher LET values due to the overkill phenomenon. To kill a cell, a sufficient energy deposit in DNA to induce adequate double-strand breaks is required. While low-LET particle radiation may be inefficient with its sparse ionization, high-LET radiation may also be ineffective for it could deposit excess energy and, consequently, lead to cellular overkilling due to its dense ionization. Naturally, optimal LET radiation produces just enough energy for cell death. Given that particles have a higher density of ionization along their tracks, possess a higher LET, and are

characterized by a shorter range in biological matter compared to photons, the likelihood of causing localized biological harm is greater, resulting in a higher value of RBE. In other words, the RBE of hadrons, when compared to X or γ-rays, is greater than unity, therefore highlighting the higher effectiveness of hadrontherapy with respect to conventional radiotherapy.

1.3.7 Oxygen Enhancement Ratio

Under oxic or hypoxic conditions, the cellular response to ionizing radiation is significantly affected. As a matter of fact, oxygen, while promoting the activity of free radicals, enhances radiation damage and reduces the radiation dose required to achieve a specific level of cell survival. This phenomenon is described through the oxygen enhancement ratio (OER) which

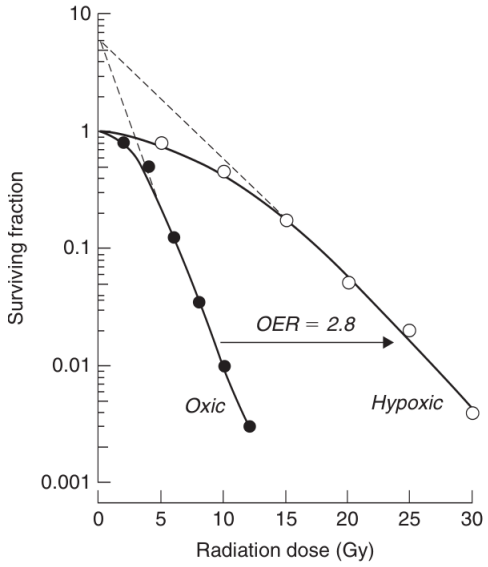

Figure 5: *As the linear energy transfer (LET) increases, the oxygen enhancement ratio (OER) decreases. This trend is depicted in the graph, where closed circles represent monoenergetic α-particles and deuterons, while the open triangle represents X-rays ([6]).*

measures the effectiveness of radiation in the presence of oxygen when compared to anoxic conditions.

$$OER = \frac{D_{hypoxic}}{D_{oxic}} \tag{1.12}$$

The oxygen effect is only observable during, or shortly after, irradiation. As oxygen tension increases, radiosensitivity rises steeply, leading to a higher OER. Radiosensitivity significan-

tly increases when oxygen tension exceeds a low threshold value, whereas elevated oxygen concentrations induce a smaller increase in radiosensitivity.

1.4 The Physics of Hadrontherapy

The interactions occurring between particles and matter are of great importance in the field of radiotherapy and hadrontherapy since it uses ionizing radiation, such as X-rays, γ-rays, protons, and other ions, to target and destroy cancerous cells. Indeed, understanding how these types of radiation interact with biological matter is crucial for optimizing protocols, limiting undesirable side effects, and advance in the effectiveness of treatment.

1.4.1 Interactions of Charged Particles in Matter

Charged nuclei mainly interact with matter through Coulomb forces. This arises from the positive charge of the particle and the negative charge of the orbital electrons within the atoms of the absorbing material. At radiation energies responses, interactions with atomic nuclei are generally considered rare occurrences[3] given that the atom has a cross-section approximately 10^{10} times larger than the nucleus.

As the charged particle travels through the absorbing medium the atomic electrons feel an impulse derived from the attractive Coulomb force depending on the distance of the particle from each electron. Based on the intensity of this interaction two possible outcomes can occur: excitation, consisting in the energetic promotion of the electron to a higher energy shell, or ionization, in which the electron gains enough energy to break free from the atom. Although the energy transferred to the electron is often a small fraction of the total energy of the crossing particle, it still manages to reduce its velocity. Moreover, charged particles possess a

[3] Although it's an unfavorable occurrence, interactions can take place with atomic nuclei through elastic collisions, leading to multiple scattering processes and resulting in a mere deflection of the particle's trajectory.

It is pertinent to recall the precise mathematical representation of the nucleus differential cross-section $d\sigma/d\Omega$ using the Rutherford formula:

$$\frac{d\sigma}{d\Omega} = \left(\frac{1}{4\pi\epsilon_0}\frac{Z_1 Z_2 e^2}{4E^2}\right)^2 \frac{1}{\sin^4\frac{\theta}{2}} \tag{1.13}$$

In this expression, Z_1 signifies the charge of the incident particle, Z_2 is the charge of the nucleus in the medium, θ is the angle of deflection, and E is the energy of the incident particle. It's important to recognize that this potential deflection carries the risk of inadvertently affecting healthy cells when targeting cancerous ones. As a result, it is preferred to target the central region of the tumor to mitigate this possibility.

defined range in a given absorber material, representing the distance beyond which they cannot penetrate. The outcomes of these interactions are either excited atoms or ion pairs that tend to recombine into neutral atoms in their equilibrium states while emitting electromagnetic radiation.

The description provided illustrates the interaction occurring via an inelastic collision, while a less common scenario is an elastic collision, where the charged particle retains its energy, thus resulting in a mere deflection.

Linear Stopping Power The linear stopping power, denoted as S, is a physical quantity that describes the kinetic energy that is lost by a particle as it penetrates through a material per unit length. This loss occurs until the particle's energy is completely depleted and its penetration is halted. S has the dimensions of MeV/m. This parameter is also referred to as specific energy loss and for particles that possess a fixed charge state it has a value described by the Bethe-Bloch formula:

$$-\frac{dE}{dx} = \frac{4\pi}{m_e\, c^2}\,\frac{n\, z^2}{\beta^2}\left(\frac{e^2}{4\pi\epsilon_0}\right)^2 \cdot B \tag{1.14}$$

where

$$B = \left[ln\left(\frac{2m_e\, c^2\, \beta^2}{I\,(1-\beta^2)}\right) - \beta^2 - \frac{\delta(\gamma)}{2}\right] \qquad and \qquad n = \frac{N_A\, Z\, \rho}{A\, M_U} \tag{1.15}$$

and m_e is the electron mass at rest, e is the electronic charge; ρ, A and Z are the atomic density, number of the absorber atoms and their relative atomic mass respectively; N_A is the Avogadro number while M_U stands for the molar mass constant; furthermore, c and ϵ_0 are the speed of light and the vacuum permittivity, whereas β represents the velocity of the primary particle in terms of c; I is the average excitation energy and ionization potential of the absorbing material; finally, the term $\delta(\gamma)$, with γ being the Lorentz factor, is a density correction that, in the limit of large values of γ, limits the logarithmic growth of energy losses.

The general trend of $\frac{dE}{dx}$ is closely related to the behavior of the factor that multiplies B. This factor is inversely proportional to $1/v^2$ and directly proportional to z^2. Consequently, a more pronounced specific energy loss is encountered either in particles possessing higher charges or

particles moving at slower velocities. In this context, it should be acknowledged that particles with reduced speeds spend a greater amount of time in close proximity to each individual atomic electron. Consequently, these electrons experience a stronger force. Studying the dependence of S on the electron density within the absorbing material, it is natural to understand that materials possessing higher atomic numbers and densities will have an increased stopping power.

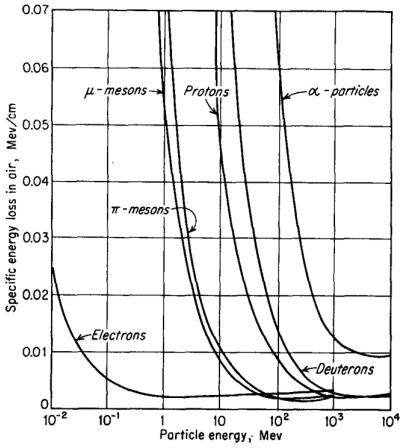

Figure 6: *Depiction of the variation of specific energy loss as a function of the energy carried by different types of particles. ([8]).*

Lastly, it's important to emphasize that the accuracy of the Bethe-Bloch formula begins to decrease at low particle energies, where charge exchange between the particle and the absorber becomes significant.

The Bragg Curve and the Energy Straggling A Bragg curve is a graphical representation that depicts the evolution of the specific energy loss along the track of a charged particle. This curve usually starts at a lower value and gradually increases as the particle proceeds through the material, interacting with atomic electrons along the way. This behaviour is consistent with the predictions made by equation (1.14), where the energy loss increases inversely with the particle's energy. Subsequently, the curve decreases as the particle approaches the end of its trajectory. During this phase, the particle's charge leads to the capture of electrons from the surrounding material, resulting in a reduction of energy loss. Right before the curve starts to decrease, one can observe the Bragg peak, which is the point along the Bragg curve where the specific energy loss reaches its maximum value. This peak coincides with the depth at which the particle comes to a near halt within the absorber. Even though possessing the same initial properties and moving in the same direction as the single particle track taken into account, a parallel beam of particles may exhibit different behaviour due to a phenomenon known as

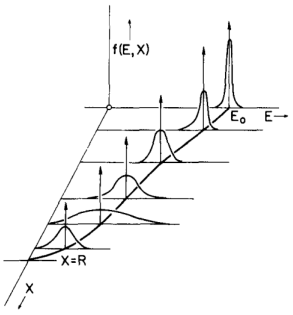

Figure 7: *Graphic representing plots of energy E for an initially monoenergetic beam of charged particles as a function of X, which is the length of the trajectory followed by the particle as it travels through the material. The contribution of energy straggling is evident in the deviations observed between the curves.*

straggling which considers the intrinsic randomness of microscopic interactions. Straggling, in particular, refers to the statistical variation in energy loss experienced by different particles with the same initial energy.

The Particle Range The average distance traveled by the particles, or the mean range, can be defined as the thickness of the material that reduces the count of the incident particles to half of its value without the absorber. Mathematically, it can be expressed as the integration of the reciprocal of the stopping power with respect to energy [4].

$$R(E_{\text{tot,in}}) = \int_{m_0c^2}^{E_{\text{tot,in}}} \frac{dE}{dE/dx} \tag{1.16}$$

Moreover, charged particles are also subjected to range straggling, a phenomenon analogous to energy straggling. In essence, even particles with the same energy may have slightly different ranges due to the inherent randomness of their interactions with the material.

Interaction of Electrons with Matter In the interaction process involving electrons and atomic electrons, a comparable scenario arises, resembling that of heavy-charged particles. However, the incident beam now consists of particles with lower masses, and electrons display a diminished rate of energy dissipation along with more intricate trajectories as they traverse absorbing materials. This complexity is attributed to the substantial deviations caused by

[4] where where $E_{\text{tot,in}}$ is the initial energy and m_0c^2 is the rest energy of the particle

collisions occurring between particles that are indeed of identical nature and, thus, identical masses.

The main distinction between the aforementioned scenario and the current one is that electrons deviate from heavy-charged particles in their susceptibility to energy depletion through both Coulomb interactions and radiative mechanisms, such as Bremsstrahlung. Bremsstrahlung, in brief, is a type of electromagnetic radiation emitted when electrons decelerate or deflect while interacting with atomic nuclei, leading to the production of high-energy photons such as X-rays or gamma rays.

The total linear stopping power for electrons coincides with the sum of collisional and radiative energy losses:

$$\frac{dE}{dx} = \left(\frac{dE}{dx}\right)_c + \left(\frac{dE}{dx}\right)_r \tag{1.17}$$

Bethe derived an expression similar to equation (1.14) to describe the ionization and excitation energy loss for the electrons, that is

$$\left(\frac{dE}{dx}\right)_c = \frac{2\pi e^4 \rho Z}{m_0 v^2}\left(ln\frac{m_0 v^2 E}{2I^2(1-\beta^2)} - ln2\left(2\sqrt{1-\beta^2} - 1 + \beta^2\right) + (1-\beta^2) + \frac{1}{8}\left(1-\sqrt{1-\beta^2}\right)^2\right) \tag{1.18}$$

while the linear energy loss through the radiative process equals the following equation

$$-\left(\frac{dE}{dx}\right)_r = \frac{\rho E Z\,(Z+1)\,e^4}{137 m_0^2 c^4}\left(4ln\frac{2E}{m_0 c^2} - \frac{4}{3}\right) \tag{1.19}$$

Moreover, the approximate ratio of specific energy losses, where E is measured in MeV units, of the two contributes is provided by

$$\frac{(dE/dx)_c}{(dE/dx)_r} \approx \frac{EZ}{700} \tag{1.20}$$

Commonly radiative losses represent a minor proportion of the overall energy losses deriving from ionization and excitation. These losses gain significance exclusively in absorber materials

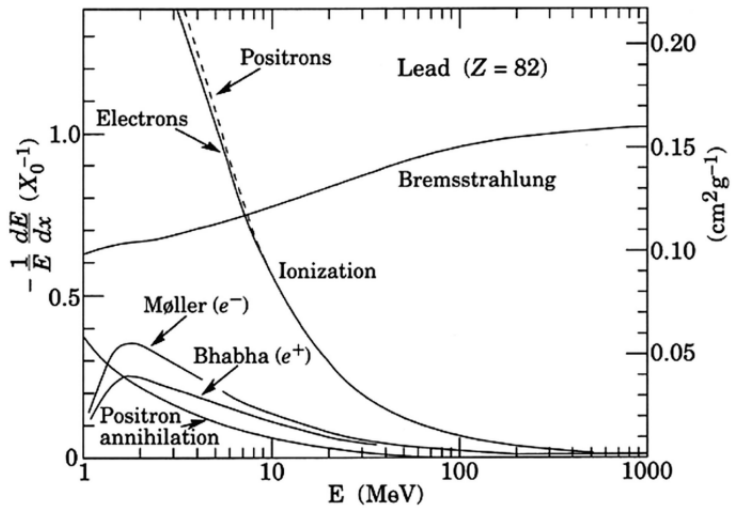

Figure 8: *Relative energy loss for Bremsstrahlung and ionization.*

characterized by a high atomic number or for high-energy electrons as it is predicted in (1.20) and as it can be seen in Figure 8.

1.4.2 Interactions of Photons with Matter

The behaviour of photons differs significantly from that of charged particles. Since they have no electric charge, photons do not engage in the many inelastic collisions with atomic electrons as previously seen. As a result of these interactions with the medium, a beam of photons does not alter its energy, but the intensity of the beam diminishes due to phenomena of scattering or absorption. Three are the processes involving the scattering or absorption of radiation in matter, that are the photoelectric effect, the Compton effect, and pair production.

The Photoelectric Effect The photoelectric effect is a phenomenon where a photon interacts with an absorber atom, transferring its energy to electrons. If the energy of the photon is sufficiently high to overcome the binding energy of the electron in the material's atomic structure, then this electron is liberated from the atom itself. The energy of the ejected photoelectron is given by:

$$E_{e^-} = h\nu - E_b \tag{1.21}$$

where h is the Planck constant, ν is the frequency of the photon and E_b is the binding energy of the electron in its original shell.

Additionally, a high-energy photo-electron is ejected from one of the atom's bound electron shells, producing a vacant spot in one of its bound shells. This vacancy is quickly filled by capturing a free electron from the medium or from the rearrangement of electrons from higher atom shells, leading the atom toward a state of greater equilibrium. As a result, X-rays are emitted, though they are typically reabsorbed close to the original interaction through photoelectric absorption.

The photoelectric process is the predominant mode of interaction for gamma rays (or X-rays) when they have relatively low energy, and this interaction becomes significantly more pronounced in materials with higher atomic numbers.

The Compton Effect Compton scattering is a process that occurs when a high-energy photon, typically within the X-ray or gamma-ray energy ranges, interacts with an initially stationary electron within an absorbing medium. During this interaction, the incoming photon undergoes a deflection by an angle θ as it imparts a portion of its energy to the electron. This energy transfer arises from the momentum exchange between the photon and the electron, leading to the ejection of the electron from its atomic shell, now referred to as a recoil electron.

The probability of Compton scattering occurring for each atom within the absorber is contingent on the availability of electrons as scattering targets, and consequently, it increases proportionally with the atomic number of the material. The angular distribution related to

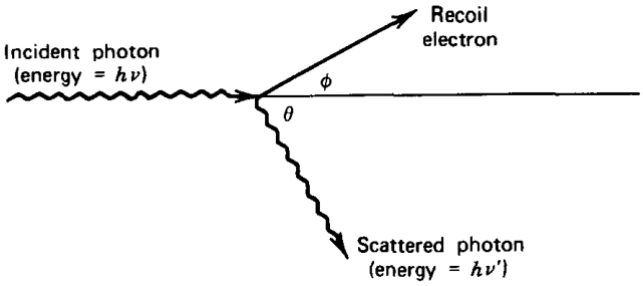

Figure 9: *Compton effect.*

the Compton scattering is described by the Klein-Nishina formula for the differential scattering cross-section.

$$\frac{d\sigma}{d\theta} = \frac{1}{2} r_e^2 \left(\frac{\lambda}{\lambda'}\right)^2 \left[\frac{\lambda}{\lambda'} + \frac{\lambda'}{\lambda} - sin(\theta)^2\right] \tag{1.22}$$

where r_e is the electron radius, while λ and λ' represent respectively the wavelengths of the incident and scattered photons.

Pair Production When referring to an energy exceeding twice the rest-mass energy of an electron, that is 1.022 MeV, pair production becomes likely to occur. This interaction takes place in the Coulomb field of the atomic nucleus. The photon annihilates with the consequent production of a pair of electron-positron, whose kinetic energy coincides with the excess energy carried by the photon with respect to 1.022 MeV. The significance of pair production rises sharply with energy.

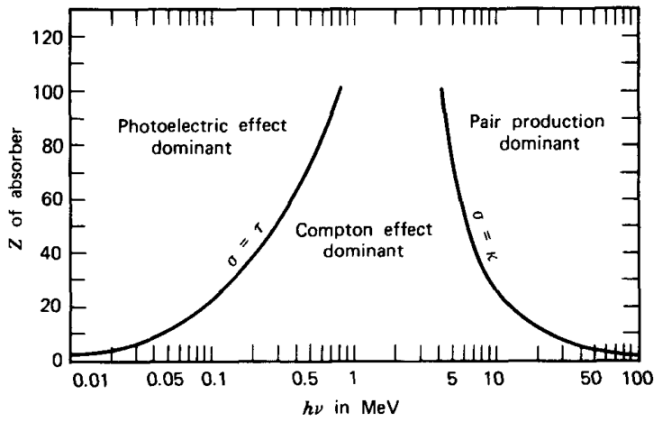

Figure 10: *Relative significance of the three major processes in the interaction between photons and matter. The lines shown represent the values of the atomic number and the photon energy for which the delimited effects are equal in occurrence. ([9]).*

Attenuation As previously mentioned, while a photon travels through a medium, its intensity gradually degrades. This phenomenon, known as attenuation, follows an exponential functional relationship with the thickness of the medium itself and follows the formula:

$$\frac{I}{I_0} = e^{-\mu t} \tag{1.23}$$

where I is the intensity of the transmitted beam I_0 is the initial intensity of the incident beam, μ is the linear attenuation coefficient of the material, and t is the thickness of the absorbing medium.

Whether considering a scattering or absorption process, each specific interaction is associated with a probability of occurrence with respect to the path length traveled by the photon within the absorber. The total probability of these effects altogether coincides with the sum of the singular specific probabilities for each. This sum, in other words, represents the probability per unit length that a photon will be removed from the beam due to either absorption or scattering and it is referred to as the linear attenuation coefficient μ.

$$\mu = \tau(photoelectric) + \sigma(Compton) + \phi(pair) \tag{1.24}$$

An important parameter that is also related to μ is the mean free path λ associated with the photon or the average distance photons have to penetrate within the absorbing material before engaging in an interaction. The mean free path can be calculated as the reciprocal of the linear attenuation coefficient:

$$\lambda = \frac{\int_0^\infty te^{-\mu t}\,dt}{\int_0^\infty e^{-\mu t}\,dt} = \frac{1}{\mu} \tag{1.25}$$

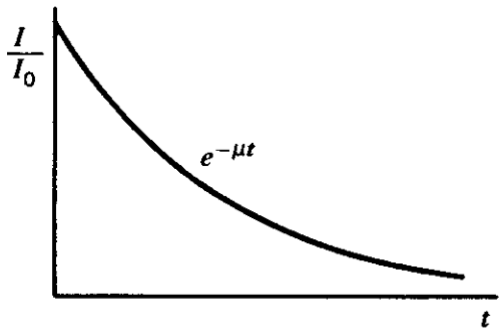

Figure 11: *Exponential photon intensity attenuation against transmission depth.*

1.4.3 Nuclear Fragmentation

When referring to the interaction between atoms and heavy-charged particles, nuclear collisions may occur when their Coulomb barrier is overcome by a sufficient amount of energy.

It's important to note that at the energies required for radiotherapy nuclear fragmentation processes become increasingly significant as particles penetrate deeper into the target. These processes predominantly entail peripheral collisions, with central collisions accounting for just 10% of the overall events. In these latter, both the projectile and the target disintegrate, typically leading to subsequent multifragmentation processes.

As shown in Figure 12, peripheral collisions involve interactions between incident heavy charged particles and the target nuclei that occur in the outer periphery of interacting particles. Thus,

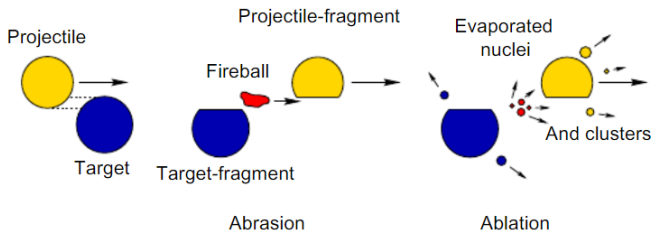

Figure 12: *Abrasion-ablation model for peripheral nuclear collisions.*

they do not delve deeply into the target nucleus. In these types of interactions, the beam particles typically do not transfer their entire energy to the target nucleus. Instead, they may lose one or a couple of nucleons, therefore contributing to the nuclear fragmentation phenomenon. This process is described by the abrasion-ablation model, in which nucleons are abraded in the overlapping zone of collision, forming a highly energetic reaction zone, often referred to as a "fireball". The residual projectile and target fragments, along with the fireball, dissipate energy through the evaporation of nucleons and light clusters. Overall, the nuclear fragmentations processes result in the production of fragments of lower and lower atomic numbers as penetration depth increases. These smaller fragments can continue to travel through the target material even after the original particles have ceased to do so, therefore having a longer particle range. In particular, in the case of projectile fragmentation, the energy of the secondary particles remains comparable to that of the original beam. However, when the fragments originate from the target, their energy is greatly reduced, causing these particles to stop shortly after their generation site.

As a result, a tail of energy deposition beyond the Bragg peak in the depth-dose profile. This tail, naturally, can hinder the effectiveness and precision of treatments. The study of the aftermath of nuclear fragmentation is a crucial step in radiotherapy, providing essential data for treatment planning and validation processes.

2. The FOOT Experiment

The FragmentatiOn Of Target (FOOT) experiment is an ambitious international effort in nuclear physics with a dual focus on advancing particle therapy and enhancing radiation protection in space. It involves more than 100 members from various esteemed institutions worldwide, including sections of the National Institute for Nuclear Physics (INFN, Italy), laboratories from the National Center of Oncological Hadrontherapy (CNAO, Italy), GSI Helmholtz Centre for Heavy Ion Research (Germany) and two institutes residing in Japan and France, as well as in the countries already mentioned.

At its core, FOOT seeks to address critical knowledge gaps in the understanding of nuclear fragmentation processes, specifically aiming to provide high-precision cross section data. This data is important for accurately estimating the physical and biological effects of nuclear fragments that are generated when energetic particle beams penetrate human tissue. As a consequence, achieving these precise measurements is crucial for refining treatment plans in particle therapy, ultimately improving the outcomes for patients. Furthermore, FOOT recognizes the vital role of these measurements in the realm of radiation protection for space missions. In space, astronauts face potential exposure to different energetic particles, including protons, helium ions, and heavier nuclei, originating from sources such as Solar Particle Events (SPEs) and Galactic Cosmic Rays (GCRs). The nuclear fragmentation of these particles can alter the space radiation spectra and contribute to the overall radiation dose astronauts receive. Thus, FOOT's work in understanding these processes is critical for designing effective shielding systems to safeguard astronauts during prolonged space missions, such as those to Mars.

FOOT's comprehensive research program covers a broad range of particle species, including protons, carbon, oxygen, and helium ions, and explores a broad spectrum of energies from 100 to 700 MeV/nucleon.

2.1 Challenges and Approaches in FOOT

As previously mentioned, the FOOT experiment is aimed at tackling the detection, tracks, and identification of the fragments produced during charged particle interactions with different

targets, specifically investigating both projectile and target fragmentation, with a significant emphasis on the latter. These secondary nuclear fragments have an extremely short range, typically just tens of micrometers (and a few electronvolts in energy), even when confronting very thin and solid targets. Consequently, they prove to be susceptible to rapid deceleration and the distortion of their energy measurement data.

To overcome these obstacles, FOOT employs an innovative approach based on inverse kinematics, through which interactions between various ion beams, such as carbon and oxygen, are examined as they collide with hydrogen-enriched targets (e.g. C_2H_4), instead of targets of comparable composition to that of biological tissue (mainly C, O, and H). In other words, when a projectile nucleus interacts with a hydrogen one within the region of the target, the resulting fragments can be analyzed by applying a suitable Lorentz boost. This transformation effectively converts the process into one resembling a collision between a proton and a target nucleus of the original projectile species, such as carbon or oxygen. While this method introduces some uncertainties related to the precision of physical quantities used for the Lorentz boost, it enables the measurement of differential cross-sections that would otherwise be extremely challenging to obtain. Additionally, a detector designed for target fragmentation measurements using the inverse kinematic approach can also directly measure fragmentation cross-sections induced by carbon, helium, and oxygen beams.

FOOT makes use of an experimental apparatus that has been created to ensure both practicality and scientific rigor. While its size has been kept compact to guarantee easy transport to research and treatment centers, it also faces rigorous precision requirements.

The ultimate goal, as a matter of fact, is to attain fragment cross-section measurements with a precision level exceeding 5%. To meet these demanding standards, the detector's charge and isotopic identification must have resolutions of 2-3% and 5% respectively. However, in the context of the inverse kinematic approach, this results in a precise resolution in reconstructed momentum, kinetic energy, and emission angle. In addition to this, to effectively reduce the adverse effects of multiple scattering and the likelihood of secondary fragmentation occurring within the target material, it is advisable to maintain a target thickness that is weighted by its overall density within the range of 2 to 4 grams per square centimeter (g/cm^2). This range helps keep the probability of fragmentation to a low level, approximately around 1%.

Moreover, considering the low likelihood of interaction and the equally low density associated with gas targets, determining cross-section data for heavy ions colliding with protons will require

a subtraction process [10], as presented below in the case of a pure target of C_2H_4 and C.

$$\frac{d\sigma}{dE_{kin}} = \frac{1}{4}\left(\frac{d\sigma}{dE_{kin}(C_2H_4)} - 2\frac{d\sigma}{dE_{kin}(C)}\right) \tag{2.1}$$

In order to optimize the detector for the experiment, particularly in terms of its geometrical acceptance, MonteCarlo (MC) simulations were conducted across the years. These simulations unveiled that heavier fragments exhibit a peak scattering angle of approximately 10 degrees, with their kinetic energy concentrated around the primary beam value. Conversely, light fragments display a wide angular dispersion and a broad distribution of kinetic energy.

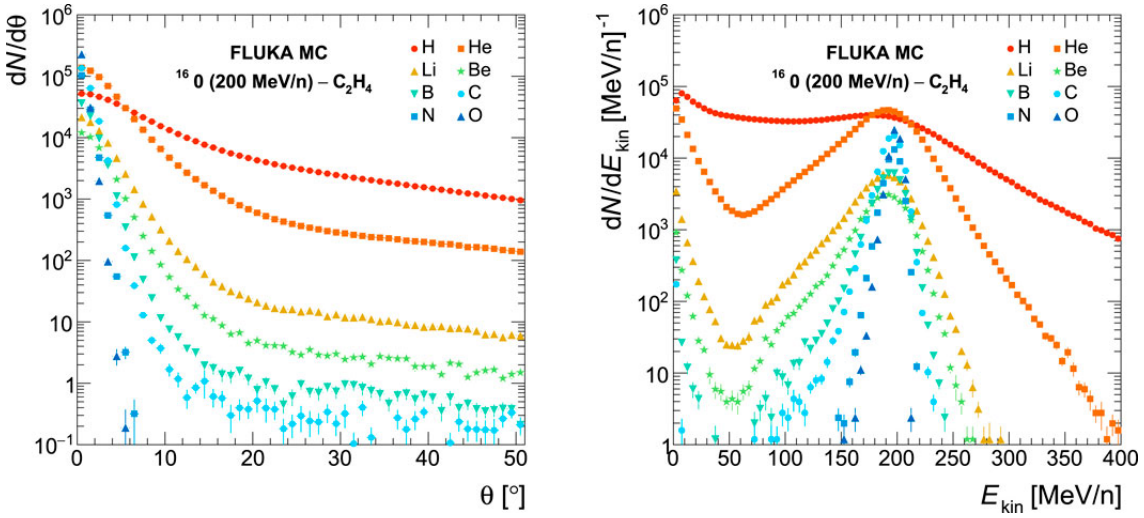

Figure 13: *On the left is the angular distribution, while on the right is the kinetic energy distribution of fragments generated when a 200 MeV/nucleon ^{16}O beam collides with a C_2H_4 target, as elaborated in [11] and presented in [12].*

To accommodate these findings, FOOT employs two detector setups: one with a magnetic spectrometer optimized for tracking fragments heavier than helium-4 (Z > 3) and encompassing a polar angle of about 10 degrees, and another based on an emulsion spectrometer for identifying lighter and low-Z fragments emitted at larger angles, reaching up to about 70 degrees. The construction of the overall apparatus and its components launched in 2018, with some already undergoing rigorous testing and calibration processes.

2.2 The Experimental Setup for Heavy Nuclei

The experimental setup for the magnetic spectrometer consists of three distinct regions, each playing a vital role in the overall process. As schematized in Figure 14, the following can be observed:

- The initial region, known as the *upstream region*, comprises the start counter and the beam monitor. It is responsible for the preliminary preparation and monitoring of the incoming particle beam, setting the stage for subsequent measurements and observations.
- The *interaction and tracking region*, centered around the target located approximately 20 to 30 cm from the Start Counter, is surrounded by a network of silicon pixel and strip detectors positioned upstream, between, and downstream of two permanent magnets. These are configured not only to facilitate fragment production but also to ensure the provision of precise momentum measurements through tracking in the magnetic field.
- The final region or *PID region* (or particle identification region) is located far from the target (at least 1 m) and consists of two orthogonal planes of thin plastic scintillator bars that provide essential information for time-of-flight measurements and energy loss. This detector is called Tof-Wall (TW). In addition to this, a BGO calorimeter placed after the TW provides data about the kinetic energy of fragments.

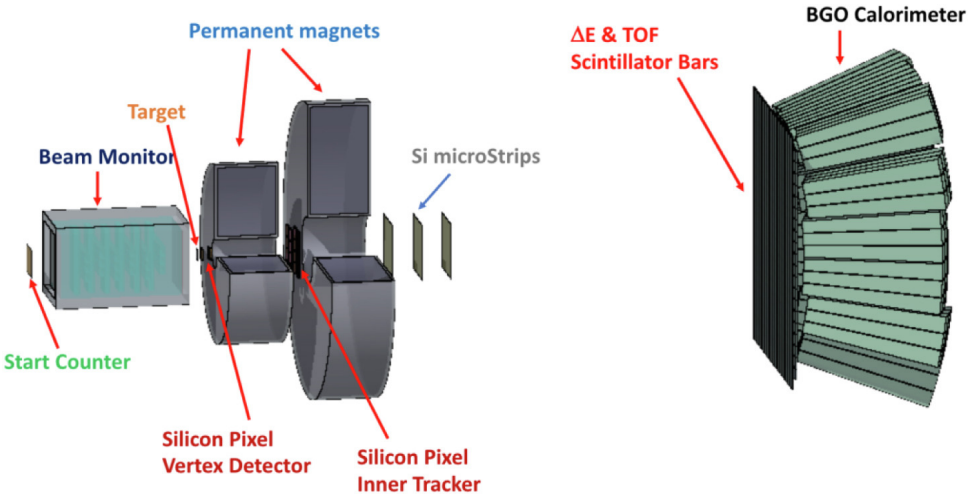

Figure 14: *FOOT detector with its components. The ion's beam progresses from left to right.*

2.2.1 The Upstream Region

The *Upstream Region* consists of preliminary and pre-target detectors, specifically designed to provide comprehensive insights into the particle beam's characteristics, including its direction and the precise point of interaction within the target. An essential goal in this region is to minimize the amount of material encountered by the beam, thus reducing the likelihood of out-of-target or multiple fragmentations. To accomplish this, two key detectors are deployed: the Start Counter and the Beam Monitor.

In simple terms, within this region, the particle beam travels through the Start Counter, an ultra-thin plastic scintillator equipped with Silicon Photomultipliers (SiPMs) for data readout, which initiates time-of-flight measurements. Subsequently, the beam progresses to the Beam Monitor, a drift chamber that meticulously tracks its trajectory, determining both direction and position with high precision, before ultimately reaching the target.

Start Counter The Start Counter (SC), called "Margarita" is positioned upstream of both the Beam Monitor (BM) and the target and is a slender, square-shaped foil with an active surface of side 5 cm that is made from EJ-228 plastic scintillator, measuring 250 µm in thickness. Such an active surface ensures the complete coverage of the typical transverse dimensions of the particle beam. Moreover, the detector is securely housed within an aluminum frame in turn enclosed by a light-tight black 3D printed box, featuring two squared windows aligned with the scintillator's field of view, sealed with a thin layer of 4 µm aluminized mylar.

A total of 48 SiPMs, each with dimensions measuring 3 x 3 mm^2, are arranged in groups of 12 on each side and further consolidated into 8 bundles of electronic channels. These SiPMs are specifically designed to capture the light emissions generated within the scintillator. Each individual channel within this configuration is assigned the responsibility of reading a chain comprising 6 SiPMs in a way that augments the detector's efficiency, a capability that proves especially valuable when dealing with a thin scintillator and the consequent generation of a relatively weak light signal.

Altogether, the Start Counter performs essential functions, such as quantifying the incoming flux of ions with extremely high efficiency (above 99%), providing a reference time for the other detectors, and executing Time-Of-Flight (TOF) measurements in conjunction with the TOF-detector, referred to as TOF-Wall (TW).

The SC delivers an impressive time resolution on the order of approximately $\sigma_t \approx 60$ps, a

measurement attained with a carbon beam possessing a kinetic energy of 700 MeV/nucleon at GSI. It's also worth highlighting that the SC's versatility allows for the use of different thicknesses, ranging from 250 µm to 1 mm, to accommodate various beam projectiles and energy ranges.

Beam Monitor Situated between the SC and the target, the Beam Monitor (BM), which was also deployed in the FIRST experiment [13], is a drift chamber consisting of 12 distinct anodic wire layers, strategically configured with wires aligned along both the x and y axes, alternating between planes. This configuration enables the reconstruction of the beam profile from both perspectives. Each layer is equipped with 3 drift cells, each with rectangular dimensions of 16 x 10 mm^2, with the longer side oriented perpendicular to the beam direction. To address potential spatial ambiguities during track reconstruction, two consecutive layers are staggered by a half-cell width [14].

The BM serves the essential function of measuring both the direction and the point of impact of the incident beam ions on the target. Furthermore, the BM helps identify events in which the beam may have fragmented within the SC, producing one or more deviated tracks. Indeed, as charged particles travel through the chamber, they ionize the gas mixture (the BM, operating at 0.9 bar, employs an 80%/20% of argon and carbon dioxide respectively) producing positive ions and electrons. The latter produce either positive or negative pulses based on their proximity to the anodic wires. The signals are then collected and processed by a reconstruction code to define the direction of the particle beam.

The BM has displayed an impressively high efficiency of approximately 90% and offers a minimum spatial resolution on the order of 100 µm in the central region of the BM cell [15]. Additionally, its swift readout time, within the microsecond range, guarantees that tracks from different events do not overlap or mix. This commitment to precision in event reconstruction, coupled with its exceptional spatial resolution, plays a vital role in precisely measuring the direction of fragments, achieving accuracy within a few milliradians.

It is important to remember this precision is indispensable for accurately determining the kinetic energy of fragments in inverse kinematic conditions, thereby meeting the stringent required resolution standards.

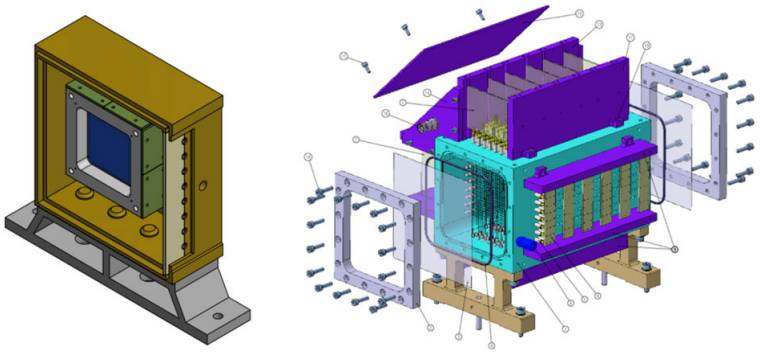

Figure 15: *Depiction of the Start Counter detector (left) and of the Beam Monitor drift chamber (right).*

2.2.2 The Tracking Region

The incident beam's journey through the *Tracking Region* unfolds as follows: it first encounters the target (TG) and then proceeds to the vertex detector (VTX). Continuing seamlessly, it enters the magnet region, traversing the Inner Tracker (ITR), and immediately after the second magnet, it traverses the Micro Strip Detector (MSD). Altogether, this entire interaction region is comprised of a magnetic spectrometer, featuring two permanent magnets and three silicon detectors—specifically, the VTX, ITR, and MSD.

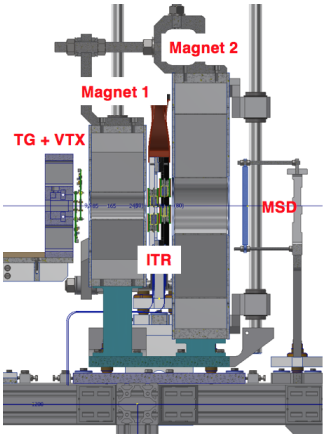

Figure 16: *Schematic view of the tracking region.*

The Vertex Detector The Vertex detector (VTX) is a versatile component capable of accommodating up to five distinct targets placed on a movable and remote-controlled tray [16]. It comprises four layers of pixel sensors aligned along the z-axis, designed to capture emitted fragments within a generous angular acceptance of about 40 degrees. These layers feature a compact 2 x 2 cm^2 transverse dimension and are strategically positioned at various distances from the central target point along the z-axis: 0.6 cm, 0.9 cm, 2.1 cm, and 2.4cm.

In pursuit of attaining standards for minimal material presence and high precision, each VTX layer adopts the MIMOSA-28 (M28), which are silicon chips belonging to the CMOS family of Monolithic Active Pixel Sensors (MAPS) technology. The M28 sensor, accompanied by an amplifier and current/voltage measurement circuitry, features a matrix of 928 rows and 960 columns of pixels, with an overall size of 20.22 x 22.71 mm^2. It employs a rolling shutter readout technique with a frame readout time of 185.6 µs.

The VTX's data readout system is realized through an Intel System-on-Chip (SoC) FPGA, housing a dual-core CPU. This FPGA manages sensor interfacing and oversees the Data Acquisition (DAQ) control framework. Additionally, to adhere to the stringent material presence requirements, all four M28 sensors are meticulously thinned down to a mere 50 µm, collectively contributing to an impressively slim material budget of only 200 µm for the entire VTX tracker.

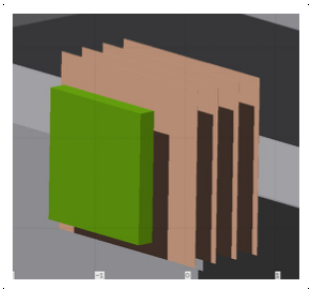

Figure 17: *TG and VTX detector view.*

This setup, coupled with the VTX's remarkable spatial resolution of 5 µm [17] and complemented by data from the BM, facilitates the attainment of milliradian-level accuracy. Finally, this configuration effectively minimizes the impact of multiple scattering.

The Magnetic System The magnetic system is of great significance within the FOOT apparatus as it bears the responsibility of altering the trajectories of the generated target fragments. To maintain both portability and achieve the requisite precision in momentum resolution while also preserving an angular acceptance of 10° for emitted fragments, a Halbach configuration employing two permanent magnets was implemented. Each magnet consists of a dozen individual units constructed from Samarium-Cobalt (SmCO), known for its ability to retain magnetic properties even in high-radiation environments. The Halbach configuration [18] adopts a structured cylindrical layout with a void surrounding the central axis, ensuring the generation of a uniform dipole magnetic field.

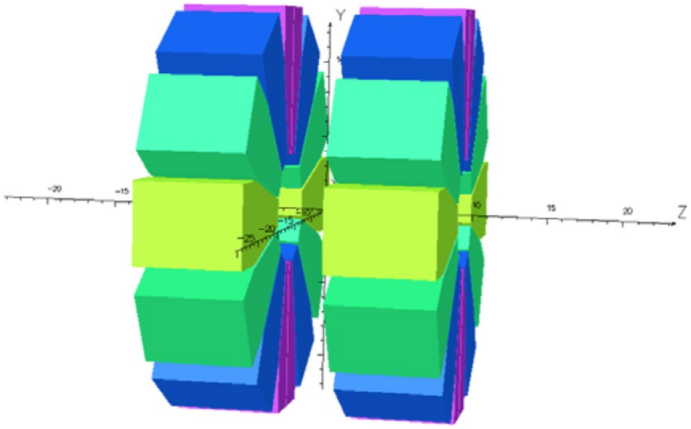

Figure 18: *Halbach configuration for the two permanent magnets.*

More specifically, the first magnet boasts a 5 cm gap diameter, while the second features a 10.6 cm gap diameter. These can generate maximum field intensities of 1.4 T and 0.9 T along the y-axis within the internal cylindrical cavity, respectively. Moreover, the inner tracker, which is positioned between the two magnets, encounters a magnetic field with an intensity hovering at approximately 0.6 T.

The generated magnetic field is exploited by the magnetic spectrometer, leading to the deflection of the trajectory of the incident charged particles due to the Lorentz force within the magnets and induced by the magnetic field itself.

$$\mathbf{F} = q\mathbf{v} \times \mathbf{B} \tag{2.2}$$

A centripetal force of the same magnitude also applies to the particle.

$$\mathbf{F} = \frac{m|\mathbf{v}|^2}{r}\hat{\mathbf{r}} \tag{2.3}$$

Upon equating the magnitudes of these two forces, the radius of curvature r is determined.

This value remains constant, since the underlying variables on which it depends remain fixed.

$$r = \frac{m|\mathbf{v}|}{q|\mathbf{B}|} \tag{2.4}$$

Based on the determined information, one can derive the magnitude of the pulse, p. Under the assumption that the magnetic field extent L is considerably smaller than the curvature radius r, the deflection angle of the trajectory can be established.

$$|\mathbf{p}| = m|\mathbf{v}| = qr|\mathbf{B}| \qquad \theta = \frac{L}{r} = L\,\frac{q\,|\mathbf{B}|}{m\,|\mathbf{v}|} \tag{2.5}$$

This leads to the calculation of the associated resolution.

$$\frac{\sigma_{|\mathbf{p}|}}{|\mathbf{p}|} = \frac{\sigma_\theta}{\theta} \tag{2.6}$$

The Inner Tracker The Inner Tracker (ITR) detector is designed to track particle fragments subject to a magnetic field while prioritizing a minimal material budget to avoid interfering with particle trajectories. The ITR employs two planes of closely spaced M28 pixel sensors, each covering 2 x 2 cm^2. Each plane altogether covers an area of 8 x 8 cm^2 and is responsible for measuring the position of the particle tracks in a direction orthogonal to the beamline and the direction of these tracks. These sensors are thinned down to 50 µm to minimize multiple scattering and maximize tracking precision. They are arranged into modules, with four sensors on each face, supported by layers of Kapton, a polyimide film. To avoid dead zones, or regions where no measurements are possible, the two sensor planes are slightly offset, so that there are no gaps in tracking coverage. The whole structure is held together by a 2 mm thick foam spacer made of silicon carbide (SiC) and mounted on a metallic frame, ensuring stability. In addition to this, Flexible Printed Cables (FPCs) connect the sensors to the outside world, allowing for power supply and data signal transmission. Indeed, the DAQ system is analogous to that of the VTX detector. However, given its larger detector area, the ITR necessitates the incorporation of a mechanical support structure, which unavoidably contributes to its overall material usage.

Regarding this matter, it's noteworthy to mention that the material budget for an individual ITR ladder is approximately 0.3% relative to the radiation length.

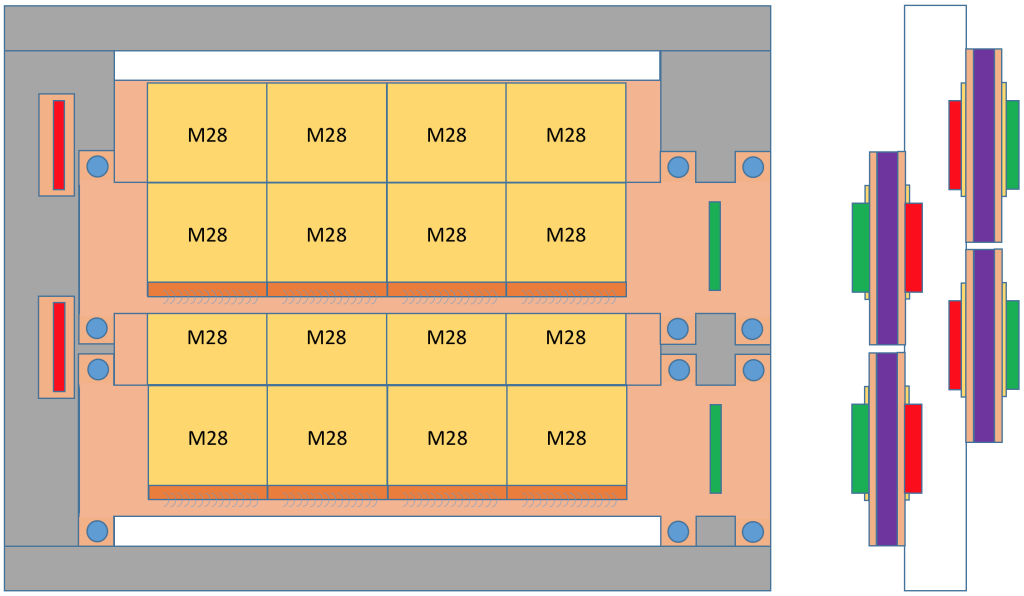

Figure 19: *Schematic image of the ITR.*

The MicroStrip Detector Positioned downstream of the second magnet, the MicroStrip Silicon Detector (MSD) is responsible for the tracking of charged particles as they exit the magnetic field. Therefore, it provides critical data for momentum determination, aligning reconstructed tracks with hits in other detectors, such as the Time-of-Flight (TOF) scintillator and calorimeter, and delivering redundant measurements of energy loss per unit length for precise particle charge identification. The MSD spans a surface of 9 x 9 cm^2 and its layered design consists of three silicon planes, each with a thickness of 150 µm, separated by a 30 µm bi-adhesive Kapton spacer that ensures the correct positioning of these layers. Each plane employs an array of 1440 closely spaced strips, set at intervals of 125 µm between their centers, allowing for high-resolution spatial (35 µm) and angular (10°) data acquisition.

2.2.3 The Particle Identification Region

The fragment identification region, positioned at a significant distance from the target, marks the final stage of the detector setup. Here, the detection process involves two orthogonal layers

of plastic scintillator bars, collectively forming the TW detector. These are designed to measure both Time-of-Flight and quantify the energy loss of the detected fragments. Subsequently, this is followed by a Bismuth Germanate (BGO) calorimeter containing inorganic scintillator crystals whose role is to precisely determine the kinetic energy of the fragments before they come to a complete halt within its confines.

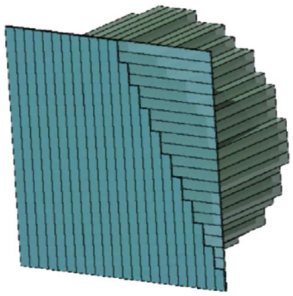

Figure 20: *Depiction of the PID region: the 20 scintillator bars placed perpendicularly and positioned in front of the matrix of inorganic crystals constituting the calorimeter are shown.*

ToF-Wall Detector The TOF-Wall detector (TW) is composed of two orthogonal x-y layers of 20 plastic scintillator bars each of which is 0.3 cm thick, 2 cm wide, and 44 cm long so that collectively the layers occupy an active area of 40 x 40 cm^2. These bars are designed to measure both the energy deposited (ΔE) and Time-of-Flight for incoming ions, aiding in charge (Z) identification. The TW's dimensions are tailored to match the angular aperture of heavy fragments at a specific distance from the target in the experimental room conditions. Moreover, the selection of the bar's thickness represents a careful balance between achieving a stronger scintillation signal, thereby an improvement in timing and energy resolution, and minimizing the risk of secondary fragmentation within the bars.

Each edge of the scintillator bars is coupled with Silicon Photomultipliers (SiPMs) for signal detection, enabling the attainment of 1024 samples so that the whole wave is recorded and stored for offline analysis.

The extensive data capture and precise timing provided by the SiPMs enable a TOF resolution [19] better than 100 ps and an energy loss resolution of $\sigma(\Delta E)/\Delta E \approx 5\%$ for heavier fragments. Additionally, the high precision time measurement aids in reconstructing hit positions along the bars with a precision of $\sigma_{pos} < 8$mm, enhancing the accuracy of fragment tracking and identification in the offline reconstruction process.

Calorimeter The FOOT calorimeter, positioned as the terminal detector, plays a pivotal role in measuring the kinetic energy of fragments, which is essential for determining their mass (A). It operates across an energy range where various phenomena occur depending on the energy of incoming fragments. At the highest energies, around 700-800 MeV/nucleon, hadronic showering prevails due to the surpassing of the pion production threshold. Achieving complete containment in the calorimeter under these conditions presents challenges due to the need for substantial size increases, resulting in reduced resolution at these energy levels.

Conversely, for studies involving target fragmentation with ions like ^{12}C and ^{16}O up to 200 MeV/nucleon, where energy loss primarily occurs through electromagnetic interactions, the calorimeter effectively contains the fragments, optimizing energy resolution. However, it's worth noting that in some events neutron production occurs, causing a portion of fragment energy to escape the detector and introducing systematic errors. FOOT mitigates this by leveraging redundant information from other detectors, given its relatively low beam intensity.

The choice of Bismuth Germanate (BGO) as the calorimeter material, owing to its high density ($\rho = 7.13$ g/cm^3) and light yield (around 10 photons per keV), aligns with FOOT's stringent performance requirements. Specifically, the FOOT calorimeter will consist of 320 BGO crystals arranged in an approximately 20 cm radius disk-like formation, with each crystal measuring 2 $\times$ 2 cm^2 on the front face and 3 $\times$ 3 cm^2 on the back face, and a length of 24 cm. These crystals will be arranged into 3 $\times$ 3 modules to facilitate handling and coupled to SiPMs matrices with a 2 $\times$ 2 cm^2 active surface and a 15 µm pitch for a linear energy response up to 10 GeV. Extensive beam tests across various energy ranges have demonstrated a highly linear response and an energy resolution consistently below 2%, meeting the experiment's requirements for heavier fragments [10], [20].

2.2.4 The Experimental Setup for Lower-Z Fragments

The experimental setup for studying lower Z (≤ 3) fragments in the FOOT experiment employs an Emulsion Spectrometer (ES). Positioned downstream of a pre-target region similar to the previous setup, the SC and BM are responsible for monitoring the incoming particle beam. An SC of 250 µm in thickness and analogous to that developed in the FIRST experiment ([13], [14]) is employed since that was originally designed for counting incoming ions and didn't require precise timing measurements. The ES function is led at its core by nuclear emulsion detectors. These combine the target material and the detection medium in a compact and self-contained

configuration, thereby disposing of the need for power supplies or complex readout systems while also ensuring a sub-micrometric spatial resolution. Indeed, it is an ideal technology for measuring differential cross-sections, especially when dealing with particles emitted at large angles.

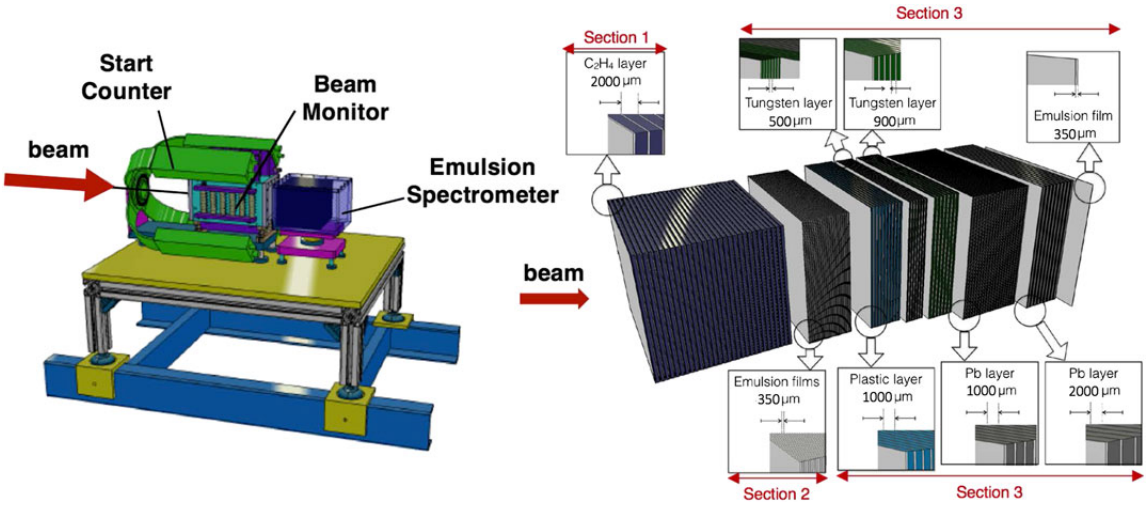

Figure 21: *On the left, the ES and its location are compared to the SC and BM. On the right, is a schematic view of the ES sections with the C2H4 target.*

The emulsion films utilized consist of two 70 µm sensitive layers placed on a plastic base of 210 µm, collectively occupying 350 µm in thickness. These layers contain AgBr crystals acting as latent image centers within an organic gelatine binder, enabling this latter to record the trajectories of charged particles.

More specifically, when charged particles reach the emulsion film, they induce ionization events within the film's crystal lattice, generating electron-hole pairs. Some electrons become trapped within lattice defects known as latent image centers, attracting silver ions (Ag^+). These trapped electrons cause Ag^+ ions to transform into neutral silver atoms (Ag). During the development of emulsion films, a developer solution aids the conversion of silver bromide crystals, containing neutral silver atoms deposited at latent image sites, into distinct solid black metallic silver grains. These are easily detectable and therefore serve as a record of the particle's trajectory.

Then, automated scanning systems [21] proceed to rapidly process the emulsions, generating large datasets while dedicated software analyzes the resulting data to identify aligned clusters of pixels and reconstruct particle tracks. As can be seen in Figure BLANK, the ES can be divided into three distinct sections based on their respective function.

Interaction and Vertexing Region The first section of the Emulsion Spectrometer (ES) serves the function of characterizing particle interactions within the experimental setup. Its structure consists of elementary cells alternating layers of the target elements, C or C_2H_4, in conjunction with emulsion films. When the incoming ion beam interacts with these cells, it generates secondary fragments that are subsequently detected by subsequent segments of the spectrometer. Finally, its length is tailored for each specific data-taking session to ensure a statistically significant number of reactions, depending on the combination of ion beam properties and the target material in use.

Charge Identification Region Charge identification works by analyzing the density of silver grains along the particle's trajectory, which is recorded in the emulsion films. Different particles with varying ionization properties leave distinct patterns of silver grains. Initially, the emulsion films undergo various thermal treatments [22], [23], altering their sensitivity to different ionizing particles. For example, some treatments erase tracks from low-ionizing particles (MIPs or Minimum Ionizing Particles) while preserving those from highly ionizing particles. This region is dedicated to charge identification for low Z fragments and each track is characterized by four track volume variables proportional to the silver grain density, each corresponding to a specific thermal treatment. By appropriately comparing these variables or using linear combinations of them, different particle charges can be differentiated.

Momentum Measurement Region Momentum measurement in the ES involves a combination of methods, specifically the range method and the Multiple Coulomb Scattering (MCS) method. This section comprises emulsion films interleaved with passive material, and its dimensions are adjusted according to the incident beam energy. The range method measures a particle's track length and estimates its momentum by correlating range with kinetic energy using reference data. The accuracy of this method depends on the composition and thickness of the passive layers within this section, which are chosen to effectively halt passing fragments.

On the other hand, MCS [24] utilizes precise measurements of a particle's trajectory, including its spatial coordinates and slope, to estimate momentum while also exploiting charge measurements from the preceding section:

$$p(MeV/c) = \frac{13.6}{\beta\delta\theta(mrad)} \cdot Z \cdot \sqrt{\frac{x}{X_0}} \tag{2.7}$$

where p, β, and Z are the momentum, velocity and charge of the fragment; x is the transversed distance, X_0 the radiation length in the material, and $\delta\theta$ the the deviation in the track's slope as it progresses along its trajectory.

By employing both the range and MCS methods the ES can determine fragment masses for isotopic identification.

However, it is worth noting that the ES operates as a one-shot detector, meaning that each dataset can be analyzed only after the ES has been assembled and exposed to particles and it cannot be reused in subsequent experiments.

3. Point Reconstruction for the MSD Analysis

The first objective of the project I have worked on is to reconstruct the MSD hit points of the FOOT apparatus from the MSD observables and classify them into two categories: true points and ghost points.

Data The project relies on FLUKA-simulated data comprising 10^6 collision events. These collision events involve a 400 Mev/u beam of oxygen nuclei striking a carbon target of 5 mm, reflecting the experimental setup (see Figure 22 for reference) utilized during the data acquisition conducted at the Darmstadt GSI (Gesellschaft für Schwerionenforschung) laboratories in 2021. These datasets were simulated using FLUKA, reconstructed by SHOE, and organized within the file `shoe_GSI2021_MC_16_O_C_400_e6_ntu.root`.

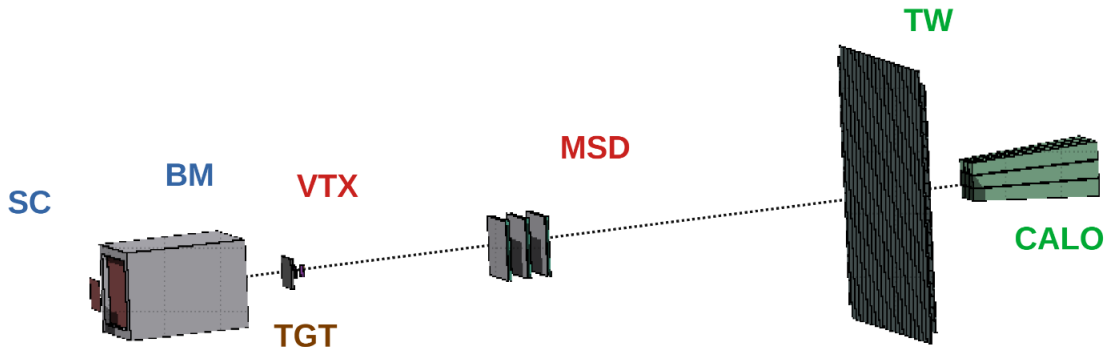

Figure 22: *Experimental electronic setup used during the data acquisition of the GSI in 2021.*

MonteCarlo simulation In the field of particle physics, and therefore hadrontherapy, the need to understand the behavior of particles as they interact with matter plays a pivotal role. One powerful tool that has emerged to address this challenge is MonteCarlo (MC) simulation, a computational technique that, in the context of the FOOT experiment, is of great significance when implemented through the simulation software package FLUKA (FLUktuierende KAskade) [25].

Developed by the INFN and the CERN, FLUKA's theory-driven framework is specifically designed for simulating the transport of particles through matter, while also incorporating

extensive libraries of cross-section data for various particle types and materials, allowing the modeling of a wide range of experimental conditions realistically.

Alongside FLUKA, operates SHOE or the reconstruction software also known as Software for Hadrontherapy Optimization Experiment. This software works on both simulated and experimental data, reconstructing particle tracks, and events. In general, details regarding the apparatus geometry, materials, and magnetic field are essential not only for FLUKA to generate simulated data, but also for SHOE. Also, ensuring that these parameters match is necessary for successful data simulation and reconstruction.

3.1 MSD Observables

Relying on the data stored in the SHOE file, a TTree, or in other words a list of independent columns or branches representing a columnar dataset, can be generated when working in the data analysis framework ROOT [26]. In terms of the project's objective, the relevant variables are the observables associated with the MSD clusters, which are listed below. Each represents a branch of the original TTree object.

```
1  Int_t ev; // event number
2
3  vector<int>* msd_clus_n;          // total cluster count for reconstructed events
4  vector<int>* msd_station_clus_id; // cluster plane identifier ranging from 0 to 5
5  vector<double>* msd_eloss;        // cluster release of energy within the specified plane
6  vector<TVector3>* msd_clus_pos;   // cluster position (x,y,z)
7
8  vector<Int_t>* msd_clus_MCId; // identifier of MC particle
9
10 // properties of the MC particle
11 vector<Int_t>* MC_FlukaID;
12 vector<Int_t>* MC_MotherID;
13 vector<Double32_t>* MC_Mass;
14 vector<Int_t>* MC_Charge;
15
```

While the variable `ev` indicates the entry of the created TTree, the most significant variables that are associated with the cluster observables are presented above and describe the following: the total number of clusters in reconstructed events, an identifier for the cluster plane, the energy loss associated with each cluster in a specified plane, and the cluster position relative

to the center of the MSD. It is important to emphasize that for clusters identifying an x-plane (clusters planes 1, 3, 5), the y-positions are automatically set to zero. Similarly, this applies to y-plane clusters (clusters planes 2, 4, 6).

The variables containing `MC` in their name are connected to information about the generated particles that genuinely passed through the detector and produced the cluster signal. As a matter of fact, each cluster is associated with a variable serving as an identifier for the reference MC particle, that is `msd_clus_MCId`. Thanks to this ID some of the properties of the MC particle can be obtained:

- `MC_FlukaID`: identifier of the type of particle that was generated;
- `MC_MotherID`: level of fragmentation in the overall decay chain;
- `MC_Mass`: mass of the particle that was generated;
- `MC_Charge`: charge of the particle that was generated.

Before proceeding with the discussion, it is useful to define some terms related to the MSD.

Cluster Denotes the microstrip hit and it is characterized by quantities related to a single plane (x or y).

Point Represents a potential actual hit and it is characterized by quantities related to two identifying planes (x and y), which are thus merged into stations.

There are a total of 6 planes and 3 stations, as can be seen in Figure 23.

3.2 The Point Reconstruction Algorithm

The algorithm used to reconstruct points from the reported clusters, organized within the ROOT TTree object, exploits a combinatorial approach. For each entry in the TTree, representing an event, the algorithm analyzes both an x and a y plane for each station. This process involves pairing specific clusters to generate individual points.

To determine the position of each point, the z-coordinate is calculated as the average of the z-coordinates of the two preceding cluster positions. It is important to note that the z-positions are fixed for the microstrip detectors.

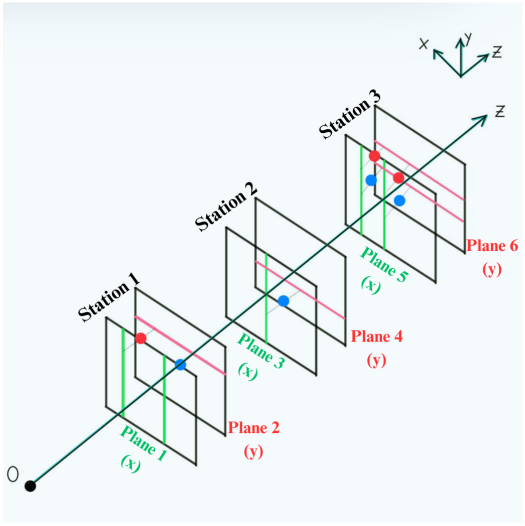

Figure 23: *Schematic view of the MSD cluster planes and stations. Points, rendered as spheres, are color-coded: blue spheres denote true points, while red spheres indicate ghost points. What is represented serves as a purely instructive illustration.*

For each x-position, a corresponding y-position is assigned, effectively creating intersections between the activated strips on the x and y planes identifying the clusters. This intersection defines a new position variable, now associated with a point and represented by its Cartesian coordinates (x, y, z).

Additionally, a variable is created to track the total energy loss associated with that point. This value is determined by averaging the energy deposited in the individual x and y plane clusters.

Finally, it is worth noting that the total number of reconstructed points is as reported in Table 1.

Table 1: *Number of reconstructed points.*

Station	Number of Points
1	1 318 167
2	1 395 281
3	1 438 229
Total	4 151 677

At this stage, it is essential to introduce two significant concepts to distinguish the newly generated points.

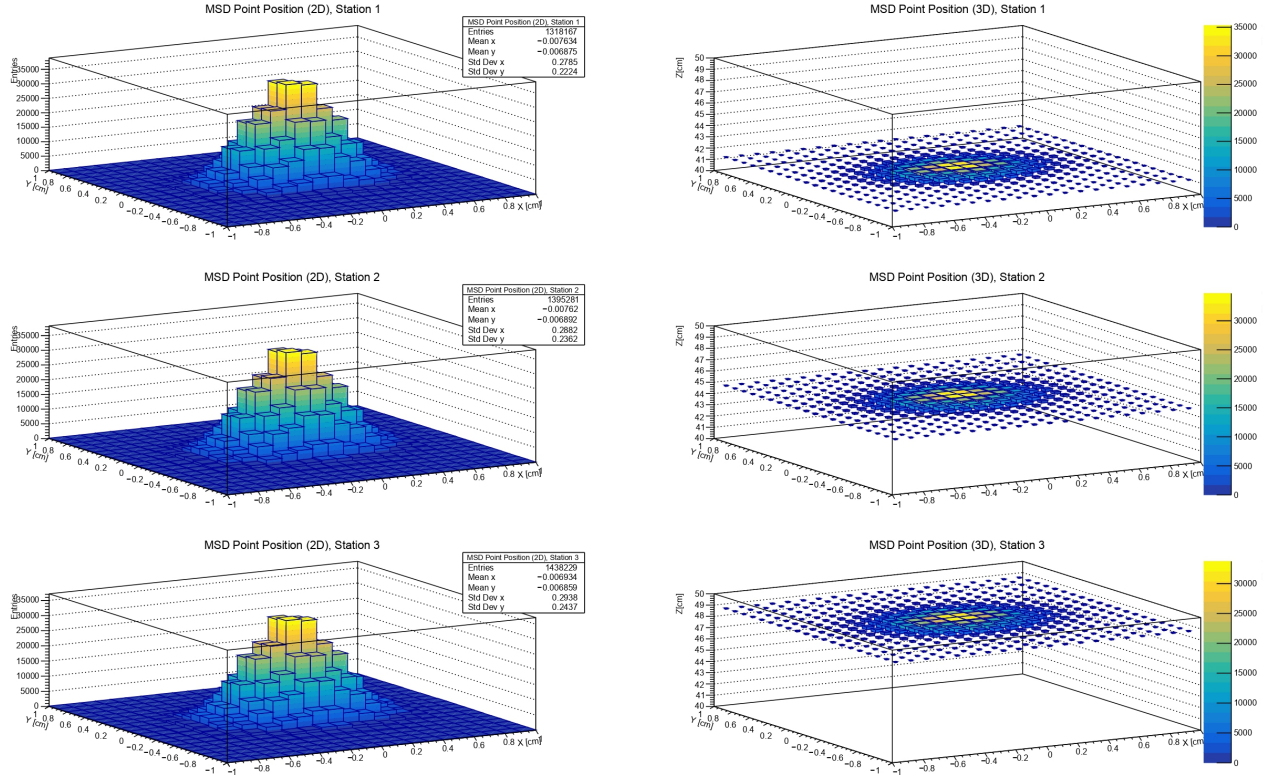

Figure 24: *MSD points position 2D and 3D distribution plots for each station.*

GHOST Points These are points formed by clusters with different MC IDs as their progenitors. Consequently, they do not uniquely represent an actually generated MC particle, as they are points that have interacted with the detector randomly.

TRUE Points Conversely, true points are those formed by clusters with matching MC IDs among their progenitors. This alignment allows us to assert that these points represent a genuinely generated MC particle.

True points correspond to particle interactions that represent the actual behavior of particles within an experiment, whereas ghost points result from uncertainties or overlapping signals, often causing confusion in identifying genuine particle tracks. Indeed, discriminant analysis can offer a solution to this problem by examining various features and properties associated with each point, creating a classification model, and implementing a discriminant cut that can accurately help distinguish between true and ghost points, while also enhancing the accuracy and reliability of particle tracking. This analysis plays a crucial role since, in the actual experiment, MC IDs and the related MC information won't be accessible.

To conclude, the quantities of efficiency ϵ and purity P shall be defined. These variables depend on the number of entities generated, both true and false, and are commonly associated with a counting algorithm and data selection.

$$\epsilon = \frac{N_{true}}{N_{generated}} \qquad P = 1 - \frac{N_{false}}{N_{true} + N_{false}} \tag{3.1}$$

where N_{true} denotes the count of genuine points that successfully pass through the specified threshold. Meanwhile, $N_{generated}$ corresponds to the total count of authentic points, and N_{false} represents the quantity of spurious points that also surpass the threshold.

Furthermore, it is essential to remember that a binomial uncertainty must be associated with the efficiency measurement [27]. This is based on the assumption that the data selection process follows a binomial distribution, with a success probability equal to the true efficiency value, which is unknown and is best estimated by the calculated efficiency ϵ. When the value of N_{true} does not fall at the limits, i.e., when it is neither zero nor equal to the total number of generated authentic points, the uncertainty can be expressed as follows:

$$\delta_\epsilon = \frac{1}{N_{generated}} \sqrt{N_{true}\left(1 - \frac{N_{true}}{N_{generated}}\right)} \tag{3.2}$$

3.3 Discriminant Analysis for Points

In the discriminant analysis of the MSD points, I have explored several associated variables derived from energy release and position. For energy-related variables, I have examined the average energy deposited on the strips of the points, the energy difference between their parent clusters, and energy dispersion. Regarding spatial variables, I have focused on the x and y coordinates, which provide insights into the point's orientation relative to the origin.

The most significant variable has been found to be the average deposited energy.

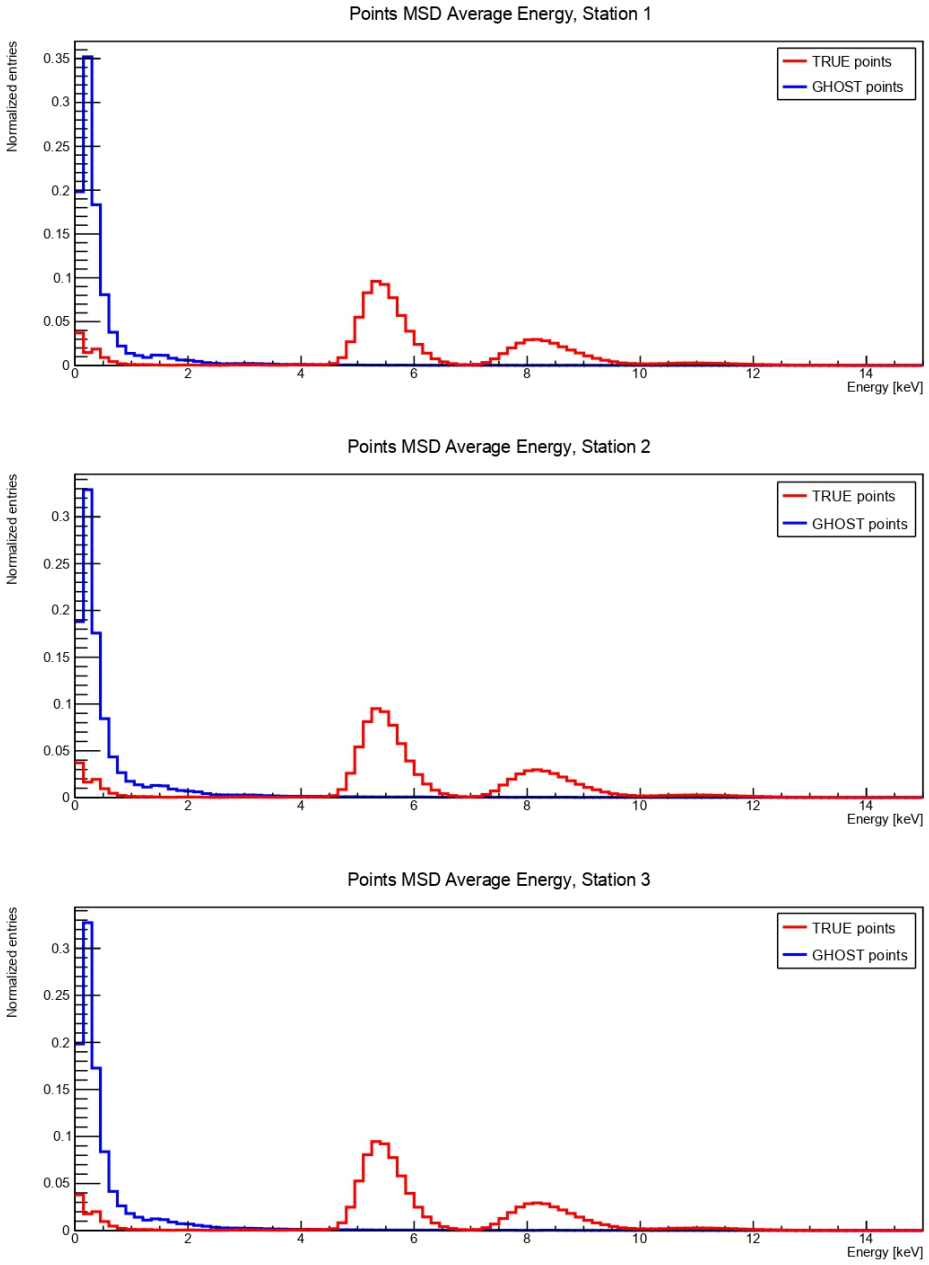

Figure 25: *Average energy distribution across the three stations of the MSD detector, with a blue line representing ghost points and a red line indicating true points.*

3.3.1 Preliminary Study of the Average Energy

In the initial part of the average energy variable analysis, plots of this variable were generated for the three stations of the MSD detector, as shown in Figure 25.

Subsequently, an integral plot of the data points was produced, yielding the results depicted in Figure 26.

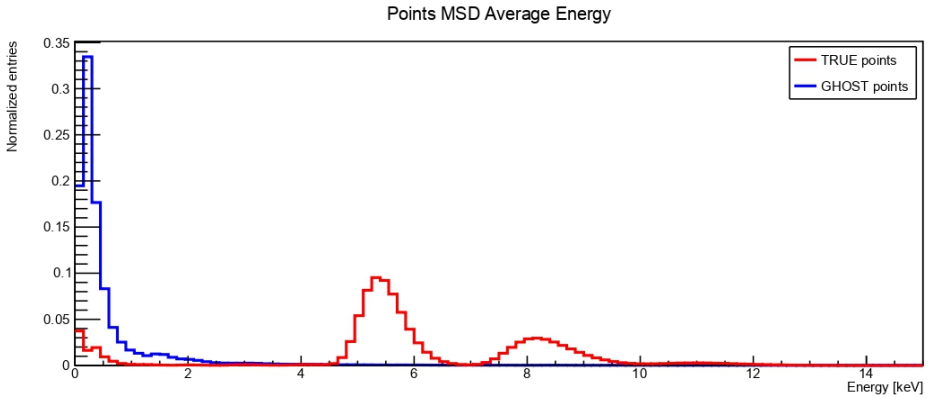

Figure 26: *Average energy distribution across all points of the MSD detector, with the blue plot representing ghost points and the red plot representing true points, as in the previous case.*

It is important to emphasize that an appropriate normalization was applied to the plots associated with ghost and true points to ensure a fair comparison between the two. Unless stated otherwise, all future plots will be normalized in the same manner.

Preliminary Counting Results The detected number of ghost and true points is presented in Table 2. It is worth noting the consistency of the data with respect to the overall number of the reconstructed points.

Table 2: *Number of ghost and true points.*

Station	True Points	Ghost Points
1	1 062 356	255 811
2	1 065 858	329 423
3	1 068 366	369 863
Total	3 196 580	955 097

Preliminary Cut at 4 keV As evident from the comparison of the four average energy plots presented, the behavior of the points is consistent across all three stations. Furthermore, it is noticeable that a potential effective cut can be implemented at the threshold corresponding to 4 keV. This cut was indeed applied, and the following counting results along with their corresponding values of efficiency and purity were obtained (see Table 3).

Table 3: *Counting Results, Efficiency, and Purity regarding 4 keV average energy cut.*

Ghost Points	True Points	Efficiency (%)	Efficiency Uncertainty (%)	Purity (%)
36 954	2 872 160	89.85	0.02	98.73

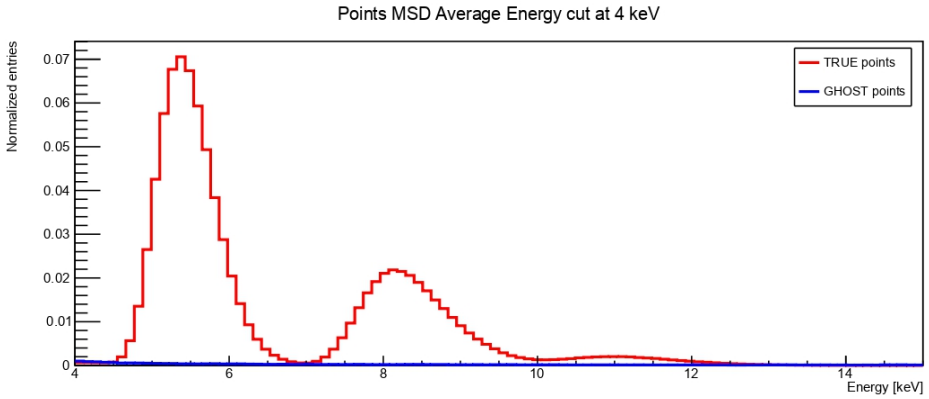

Figure 27: *Preliminary cut applied on the integral plot of the average energy variable.*

3.3.2 Study of the Average Energy on Charge

Although this may be a potentially satisfactory outcome, it is imperative to delve into the nature of the fragments being examined. Specifically, it is important to determine whether there is a significant deviation regarding heavy fragments, particularly concerning oxygen and carbon. If such a scenario arises, a different approach should be considered in data selection.

To address this, the characterization was initiated by plotting the integral average energy as a function of charge, as depicted in Figure 28.

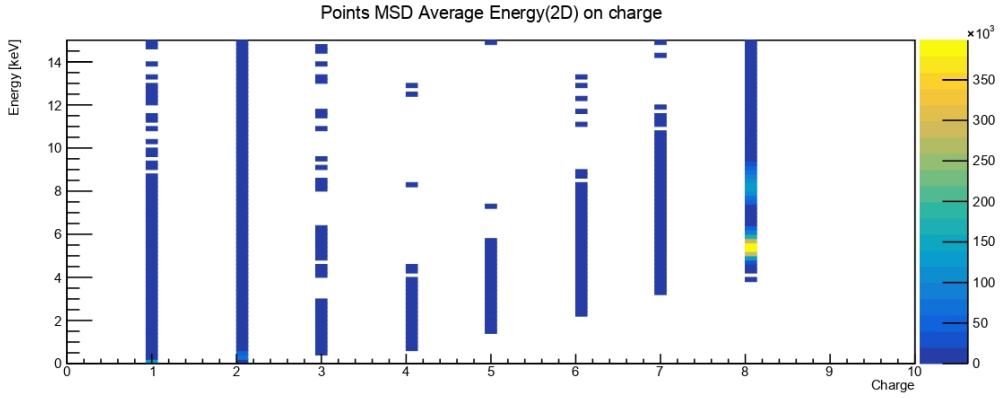

Figure 28: *2D plot illustrating the relationship between the average deposited energy and charge for each data point; colors represent data entries across the entire MSD dataset.*

Thereafter, points were categorized based on their charge, and the average energy was graphed accordingly. Similar to the previous scenario, both individual station plots and an integral MSD plot were generated, as shown in Figure 29 and 30 respectively. In addition, it is worth noting that no normalization was performed to ensure clear visibility of the results.

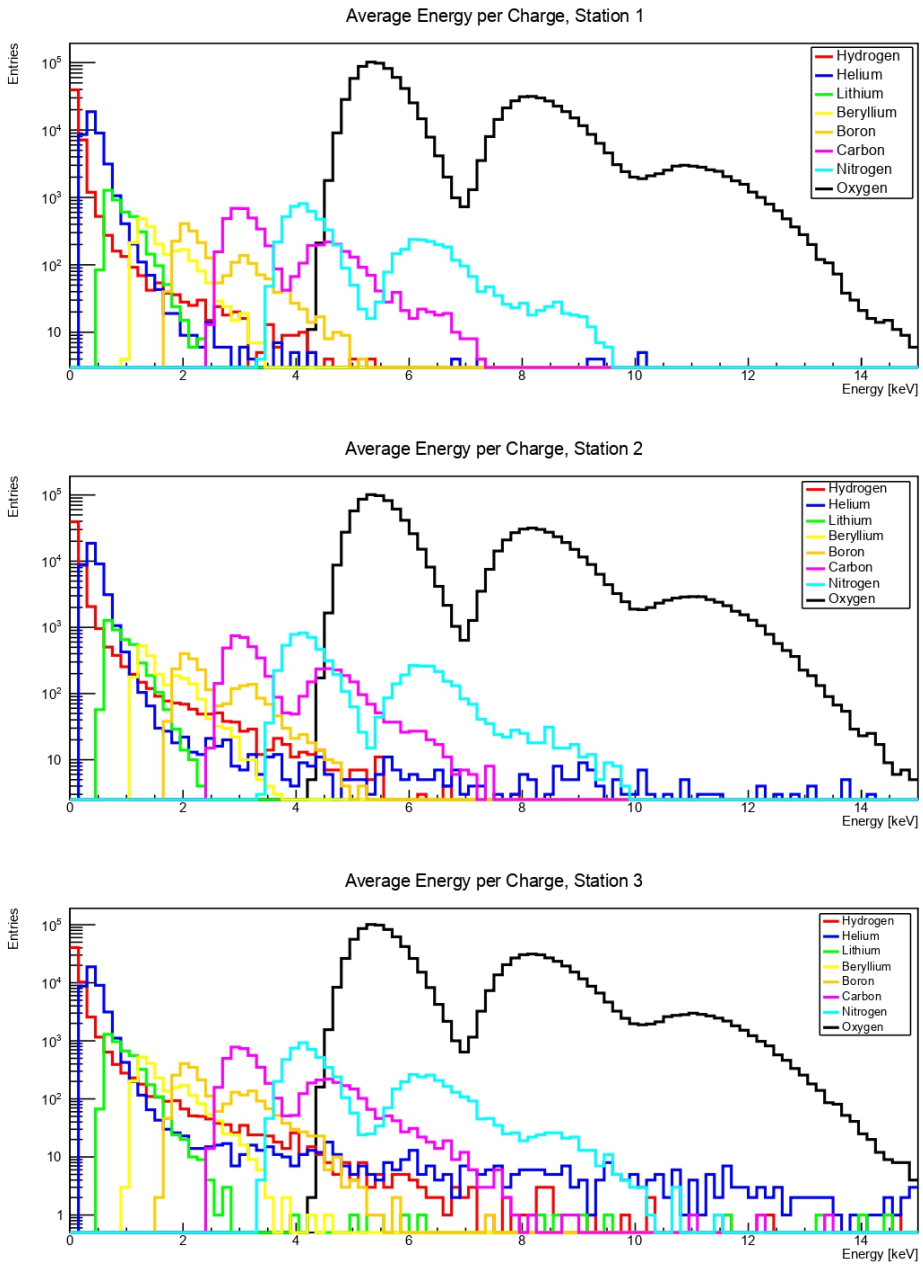

Figure 29: *Average energy distribution for each associated charge per MSD station.*

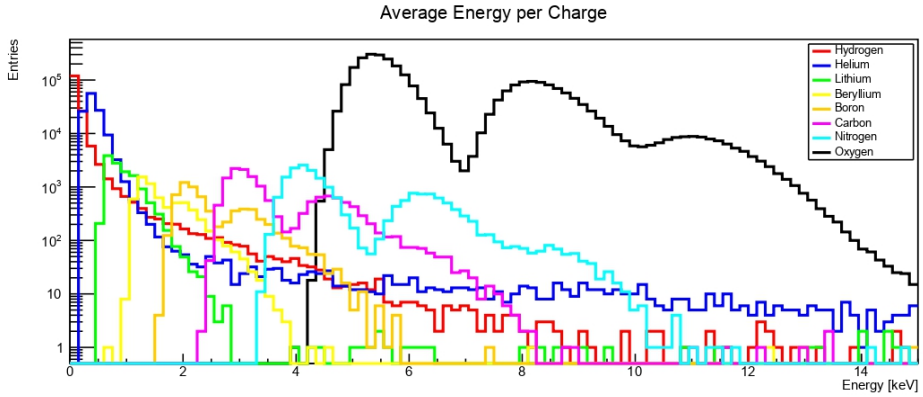

Figure 30: *Average energy distribution for each associated charge across all three stations.*

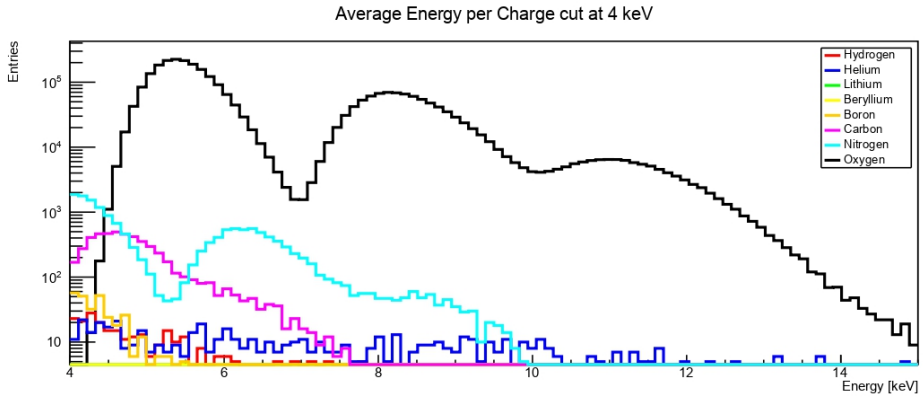

Figure 31: *Average energy distribution for each associated charge cut at 4 keV. Note that, for example, two-thirds of the carbon ions do not surpass this threshold.*

By applying the same cut discussed in the previous paragraph, it becomes evident that a significant portion of heavy ions does not exceed the required threshold, at 4 keV (see Figure 31). Therefore, it is possible to lower this threshold to 2 keV to achieve a more satisfactory result in this context, obtaining what can be seen in Figure 32 and 33.

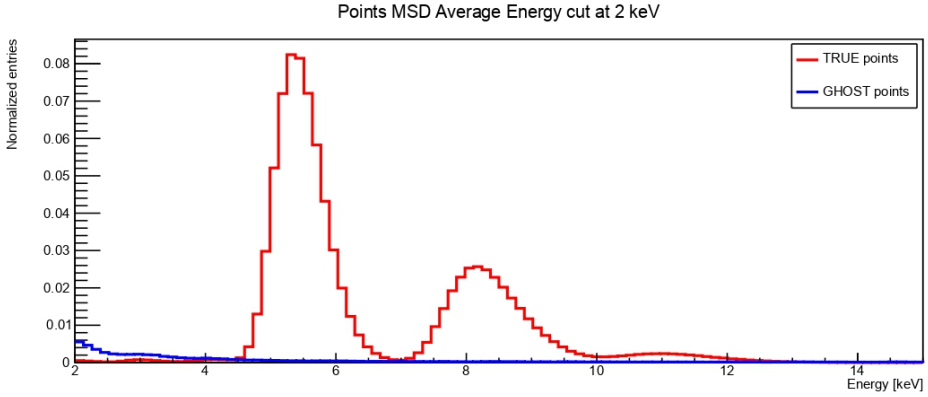

Figure 32: *Points average energy plot with new threshold at 2 keV.*

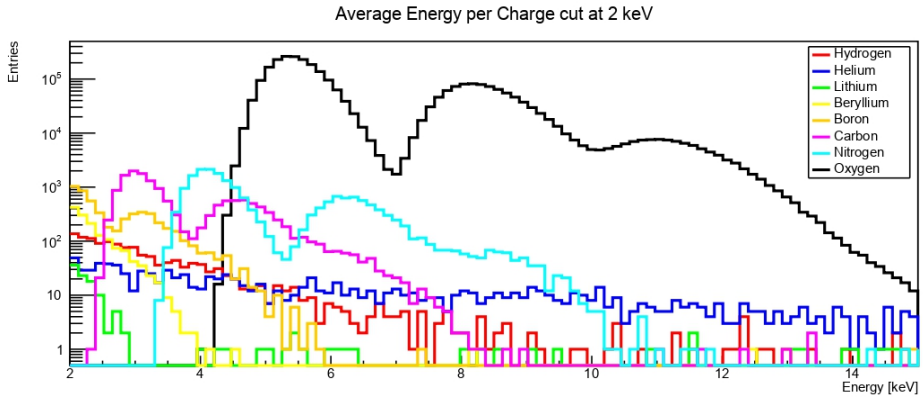

Figure 33: *Average energy distribution for each associated charge cut at 2 keV.*

The newly selected threshold yields the following counting parameters, efficiency, and purity, as reported in Table 4. Upon comparing the parameters with those obtained previously, it can be concluded that, ultimately, there is a marginal increase in efficiency, accompanied by a similarly minor decrease in purity.

Table 4: *Counting Results, Efficiency, and Purity regarding 2 keV average energy cut*

Ghost Points	True Points	Efficiency (%)	Efficiency Uncertainty (%)	Purity (%)
71 481	2 894 120	90.54	0.02	97.59

4. Track Reconstruction for the MSD Analysis

The second objective of the project I have worked on is to reconstruct MSD tracks within the FOOT apparatus using the previously reconstructed MSD points. These tracks are then categorized into four distinct groups based on their composition: tracks composed of three true points, tracks with two true points and one ghost point, tracks with one true point and two ghost points, and tracks with three ghost points.

4.1 The Track Reconstruction Algorithm

To reconstruct the tracks, I utilized a `track` class characterized by the following variables:

```
Int_t event; // number event

Double32_t avEnergy;     // average energy
Double32_t deltaEnergy;  // average energy difference between the progenitor clusters
bool isGhost;            // true if the track is associated with three ghost points
Int_t numberTrue;        // number of true points constituting the particle track


// variables filled exclusively for tracks containing at least one true point
Int_t particleID; // MC ID connected to the points, and thus the parent clusters
Int_t flukaID;
Int_t motherID;
Int_t charge;  // selected such that it is not superior to 8
Double32_t mass;

// points constituting the track per station
TVector3 P1;
TVector3 P2;
TVector3 P3;

```

The track consists of three points, one for each station. Similar to the previous algorithm, this one employs a combinatorial approach, but it's more computationally intricate as it operates across three stations.

For each track category, the algorithm seeks the next point in the subsequent station with the smallest y-distance from the previous one. If the next point is expected to be true, an additional condition is imposed: it must share the same MC ID as the original true point. Conversely, if a ghost point is anticipated next, the sole requirement is that the two parent clusters of that point must differ. In cases where points have an equal minimum y-distance, resulting in multiple equiprobable next points, tracks are generated for each one of them.

When there is no match in MC ID or ghost points, the position of that track point is automatically set to zero. Any tracks containing at least one point with any Cartesian variable equal to zero are excluded from further analysis. In parallel with position data, auxiliary variables of the custom-created class `track` are also populated to simplify track information storage.

In conclusion, for each of the mentioned track categories, a vector of the `track` type, containing a number of elements equal to the number of events, is created and then stored in a TTree for efficient retrieval of data.

Below are the numbers of the tracks obtained in the various listed categories, as shown in Table 5. It is also noteworthy that, in the implementation of the track composed of three true points, points belonging to the same particle were considered due to a time constraint.

Table 5: *Track counting results for the four categories of reconstructed tracks.*

Category	Number of tracks
True (three true points)	1 470 762
2 True + 1 Ghost	722 330
1 True + 2 Ghost	3 646 652
Ghost (three ghost points)	19 021 976

4.2 Discriminant Analysis for Tracks

In a similar manner to the previous case, energy-related and spatial-related variables were examined. In addition, a two-dimensional linear regression was performed for each calculated track on the xz and yz planes. Significant parameters, such as χ^2, intercept, and slope, were extracted from the fitting conducted using ROOT. The slope, in particular, was utilized to determine the angles of inclination of the tracks relative to the fixed origin.

The data resulting from the fitting were stored in an additional custom-made class `fit_track`, that is similar to the previous one, and subsequently placed into other TTree objects to ensure simplified data access.

Following this, plots for all four categories of tracks were generated and then compared after appropriate normalization.

4.2.1 Average Energy Analysis

The resulting plot, as seen in Figure 34, is clearly not significant for discriminating between true, false, and mixed tracks. Therefore, it will be necessary to search for other meaningful parameters for this purpose.

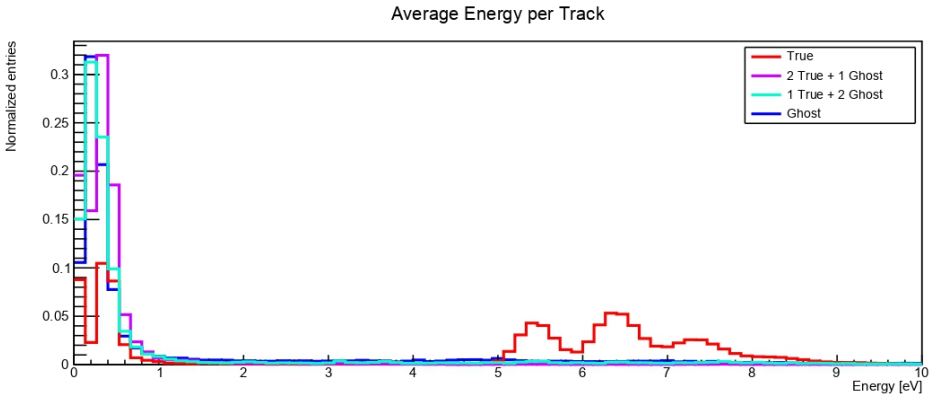

Figure 34: *Average energy distribution per track.*

Nonetheless, examining the energy distribution, particularly in relation to tracks, as it varies with the charge of the generated particle, presents an intriguing aspect for analysis.

It's evident that the oxygen tracks predominate over the others (see Table 6), followed by helium and hydrogen respectively.

Furthermore, Figure 35 provides a clear demonstration that it is possible to distinguish the energy deposition charges for each individual reconstructed track since the peaks for each charge are clearly visible.

4.2.2 Linear Regression Analysis

Below, the outcomes of the study on parameters derived from the linear regression of each analyzed track are presented. With some exceptions, such as the intercept associated with the

Table 6: *Number of reconstructed tracks based on their charge.*

Charge	Number of tracks
Hydrogen (1)	167 274
Helium (2)	314 625
Lithium (3)	16 524
Beryllium (4)	7963
Boron (5)	4231
Carbon (6)	6099
Nitrogen (7)	6279
Oxygen (8)	947 637

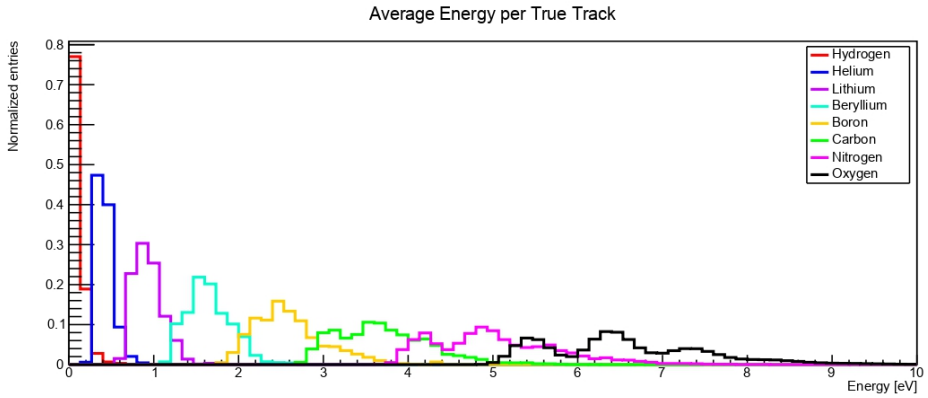

Figure 35: *Average energy distribution with normalized entries per true track; true tracks are categorized based on their charge.*

yz plane regression, it can be asserted that these parameters may serve as potentially effective discriminant factors.

The most significant parameter appears to be the one related to the y-intercept when extending the tracks constructed on the xz plane. Two cuts were applied to this parameter (see Figure 37), one more restrictive than the other, and they yielded the following results.

As expected, the mixed track composition terms do not carry significant weight. At last, it can be said that with the applied cuts, it is possible to discard the majority of ghost tracks, although a notable number of them still remains. Efficiency and purity parameters will consequently be 92.27%, with an associated uncertainty of 0.02%, and 42.34% respectively.

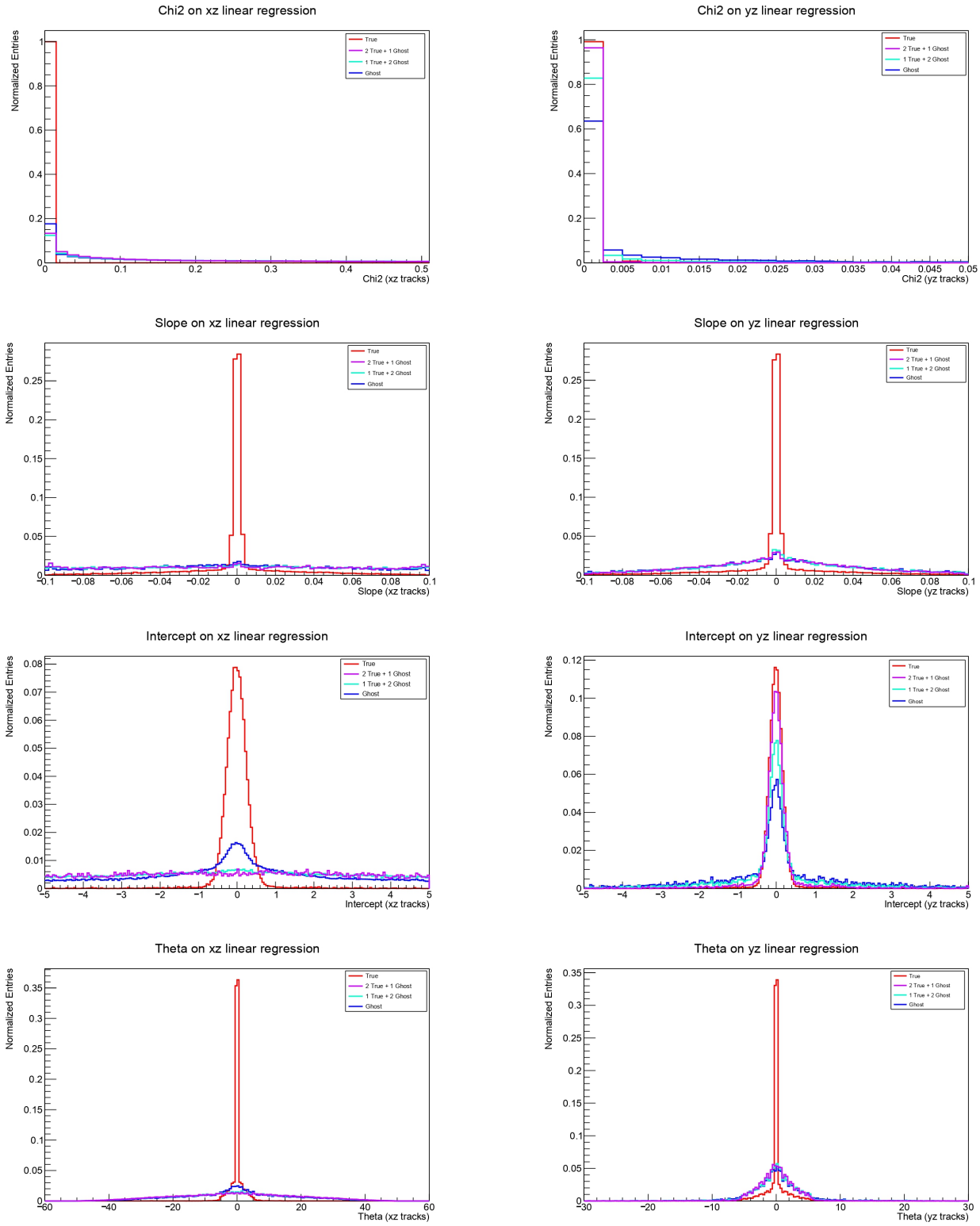

Figure 36: *Plots of characteristic parameters obtained from the linear regression on each track in the planes xz and yz.*

Table 7: *Threshold (on the intercept), track category, and counting results*

Threshold	Track category	Number of tracks
between -1 and 1	True	1 430 110
	2 True + 1 Ghost	40 167
	1 True + 2 Ghost	252 490
	Ghost	2 885 960
between -0.5 and 0.5	True	1 357 020
	2 True + 1 Ghost	19 522
	1 True + 2 Ghost	133 104
	Ghost	1 848 160

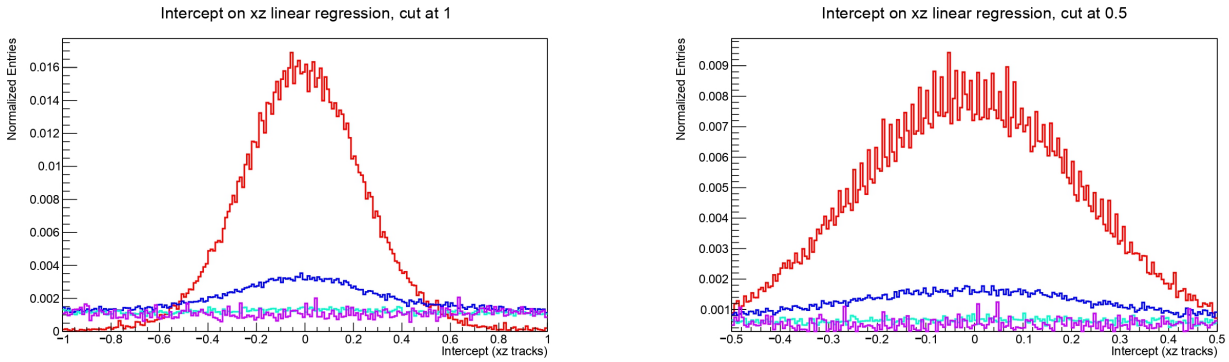

Figure 37: *Cut applied to the intercept y on the reconstructed xz tracks; respectively with thresholds between -1 and 1, and -0.5 and 0.5 .*

Conclusion

My contribution to this project mainly focused on computational analysis, since my aim was to study the reconstruction of points and tracks within the MSD detector as part of the FOOT experiment, whose main purpose is to improve hadrontherapy, namely by studying the interactions of the particle beams with the nuclei of the human body.

Regarding the reconstruction of points, the implemented algorithm focused on performing data selection to discriminate between ghost and true points, primarily utilizing the average energy deposited in the strips associated with these points. By applying a selection cut to the latter, initially, an efficiency of 89.85% and a purity of 98.73% were achieved. Further analysis involved studying the energy deposition as a function of the charge of the generated MonteCarlo particles. A slight correction was applied by shifting the selection threshold on the energy deposited in the strip from 4 keV to 2 keV, resulting in efficiency and purity values of 90.54% (and its uncertainty of 0.02%) and 97.59%, respectively.

Concerning the tracking of reconstructed points, the utilized algorithms first dealt with track reconstruction using a combinatorial approach. Subsequently, a data selection analysis, similar to the previous one, was conducted. In this case, however, the main discriminant variables were the characteristic parameters of the linear fit performed on both the xz and yz planes for each reconstructed track. It is important to note that the tracks of true points contained points associated with a single particle. This choice was driven by time constraints and it was possibly limited the spectrum of true tracks available in the study. Nevertheless, a substantial reduction of false tracks was achieved, obtaining an efficiency of 92.27% (with an associated uncertainty of 0.02%) and a purity of 42.34%. In addition to this, regarding the study of the average energy deposited on the strips, it has been observed that it is possible to differentiate charges based on the deposited energy, as shown in Figure 35.

In conclusion, it emerges from the results that, while satisfactory outcomes were achieved for the MSD points, it may be necessary to explore further options or reconsider the study's assumptions regarding the reconstructed tracks.

Bibliography

[1] «Particle Therapy Co-Operative Group». (2023), indirizzo: `https://www.ptcog.site/`.

[2] R. A. Weinberg e R. A. Weinberg, *The biology of cancer*. WW Norton & Company, 2006.

[3] J. A. Imlay e S. Linn, «DNA damage and oxygen radical toxicity», *Science*, vol. 240, n. 4857, pp. 1302–1309, 1988.

[4] R. Protection, «ICRP publication 103», *Ann ICRP*, vol. 37, n. 2.4, p. 2, 2007.

[5] M. C. Joiner e A. J. van der Kogel, *Basic clinical radiobiology*. CRC press, 2018.

[6] G. Barendsen, «RESPONSES OF CULTURED CELLS, TUMOURS, AND NORMAL TISSUES TO RADIATIONS OF DIFFERENT LINEAR ENERGY TRANSFER.», Health Research Organization TNO, Rijswijk, Netherlands, rapp. tecn., 1968.

[7] G. F. Knoll, *Radiation detection and measurement*. John Wiley & Sons, 2010.

[8] A. Beiser, «Nuclear emulsion technique», *Reviews of modern physics*, vol. 24, n. 4, p. 273, 1952.

[9] R. D. Evans e R. Evans, *The atomic nucleus*. McGraw-Hill New York, 1955, vol. 582.

[10] L. Scavarda, «The foot experiment: measuring proton and light nuclei fragmentation cross sections up to 700 MeV/A», *Bulletin of the Russian Academy of Sciences: Physics*, vol. 84, pp. 480–484, 2020.

[11] A. Ferrari, J. Ranft, P. R. Sala e A. Fassò, *FLUKA: A multi-particle transport code (Program version 2005)*. Cern, 2005.

[12] G. Battistoni, M. Toppi e V. Patera, «Measuring the impact of nuclear interaction in particle therapy and in radio protection in space: the FOOT experiment», *Frontiers in Physics*, vol. 8, p. 568 242, 2021.

[13] M. Toppi, Z. Abou-Haidar, C. Agodi et al., «Measurement of fragmentation cross sections of C 12 ions on a thin gold target with the FIRST apparatus», *Physical Review C*, vol. 93, n. 6, p. 064 601, 2016.

[14] Z. Abou-Haidar, C. Agodi, M. Alvarez et al., «Performance of upstream interaction region detectors for the FIRST experiment at GSI», *Journal of Instrumentation*, vol. 7, n. 02, P02006, 2012.

[15] Y. Dong, S. Gianluigi, C. Sofia et al., «The Drift Chamber detector of the FOOT experiment: Performance analysis and external calibration», *Nuclear Instruments and Methods in Physics Research Section A: Accelerators, Spectrometers, Detectors and Associated Equipment*, vol. 986, p. 164 756, 2021.

[16] R. Rescigno, C. Finck, D. Juliani et al., «Performance of the reconstruction algorithms of the FIRST experiment pixel sensors vertex detector», *Nuclear Instruments and Methods in Physics Research Section A: Accelerators, Spectrometers, Detectors and Associated Equipment*, vol. 767, pp. 34–40, 2014.

[17] E. Spiriti, C. Finck, J. Baudot et al., «CMOS active pixel sensors response to low energy light ions», *Nuclear Instruments and Methods in Physics Research Section A: Accelerators, Spectrometers, Detectors and Associated Equipment*, vol. 875, pp. 35–40, 2017.

[18] C. Sanelli, «Studio di fattibilità dei magneti in configurazione "Halbach" dello spettrometro dell'esperimento FOOT», Laboratori Nazionali di Frascati, INFN - Istituto Nazionale di Fisica Nucleare, INFN-17-10/LNF, mag. 2017. DOI: 10.13140/RG.2.2.13736.98568.

[19] M. Morrocchi, E. Ciarrocchi, A. Alexandrov et al., «Development and characterization of a ΔE-TOF detector prototype for the FOOT experiment», *Nuclear Instruments and Methods in Physics Research Section A: Accelerators, Spectrometers, Detectors and Associated Equipment*, vol. 916, pp. 116–124, 2019.

[20] L. Scavarda, «Design and performance of the Calorimeter for the FOOT experiment», *Il nuovo cimento C*, vol. 43, n. 4-5, pp. 1–7, 2020.

[21] A. Alexandrov, A. Buonaura, L. Consiglio et al., «A new fast scanning system for the measurement of large angle tracks in nuclear emulsions», *Journal of Instrumentation*, vol. 10, n. 11, P11006, 2015.

[22] G. De Lellis, S. Buontempo, F. Di Capua et al., «Emulsion Cloud Chamber technique to measure the fragmentation of a high-energy carbon beam», *Journal of Instrumentation*, vol. 2, n. 06, P06004, 2007.

[23] G. De Lellis, S. Buontempo, F. Di Capua et al., «Measurement of the fragmentation of Carbon nuclei used in hadron-therapy», *Nuclear Physics A*, vol. 853, n. 1, pp. 124–134, 2011.

[24] N. Agafonova, A. Aleksandrov, O. Altinok et al., «Momentum measurement by the multiple Coulomb scattering method in the OPERA lead-emulsion target», *New Journal of Physics*, vol. 14, n. 1, p. 013 026, 2012.

[25] FLUKA Collaboration. «FLUKA». (2023), indirizzo: http://www.fluka.org/fluka.php.

[26] CERN. «ROOT». (2023), indirizzo: https://root.cern/.

[27] M. Paterno, «Calculating efficiencies and their uncertainties», 2004.